Journal of Hydrology 664 (2026) 134205

Contents lists available at ScienceDirect

Journal of Hydrology

journal homepage: www.elsevier.com/locate/jhydrol

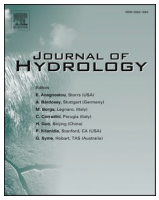

Research papers

Importance of bedrock hydrology for the rainfall–runoff process in a forested mountain catchment

Toshiaki Kameyama [a,*], Tomo'omi Kumagai [a,b], Tomohiro Egusa [c], Hiroki Momiyama [d]

[a] Graduate School of Agricultural and Life Sciences, The University of Tokyo, Tokyo 113-8657, Japan
[b] Water Resources Research Center, University of Hawai'i at Mānoa, Honolulu 96822, USA
[c] Faculty of Agriculture, Shizuoka University, Shizuoka 422-8529, Japan
[d] Forestry and Forest Products Research Institute, Forest Research and Management Organization, Tsukuba 305-8687, Japan

ARTICLE INFO

This manuscript was handled by A. Bardossy, Editor-in-Chief, with the assistance of Szilágyi József, Associate Editor

Keywords:
Bedrock permeability
Aquifer
Soil moisture
Low flow
Bayesian inference
Water balance model

ABSTRACT

Physically based, distributed hydrology–vegetation models are promising tools to understand the rainfall–runoff process, a complex system involving numerous interactions between hydrological components such as soil, bedrock, topography, vegetation, and atmosphere. Although the influence of bedrock groundwater dynamics on the water yield from headwater catchments has been demonstrated, its mechanisms remain poorly described in physically realistic runoff generation models. Here, we developed a distributed hydrological model aggregating soil and bedrock blocks with explicit water balance calculations for both the soil and bedrock modules, based on the Buckingham–Darcy law. Thus, our mechanistic model allows for direct evaluation of the importance of bedrock groundwater flow for catchment runoff generation. We validated the model against comprehensive observations of runoff, bedrock groundwater table, soil water retention, and hydraulic conductivity acquired in a forested mountain catchment of the Kanto region, Japan, in 2010–2017. Because of its ability to explicitly calculate spatiotemporal variations in the bedrock groundwater table depth, the model successfully reproduced the catchment baseflow. Refining the analysis, we demonstrated that accounting for bedrock hydrology was necessary to correctly evaluate soil water dynamics. From our model simulation, we inferred that bedrock groundwater, recharged by rainwater infiltration, dominated catchment runoff generation during low-flow periods. Insights from our catchment hydrology study should be extremely useful to optimize forest watershed management strategies toward water resource sustainability.

1. Introduction

Mountain water resources derive from the balance between runoff from catchments and water use by vegetation and are essential for billions of people globally (McDonnell et al., 2018; Viviroli et al., 2020, 2007). Rainfall–runoff processes in headwater catchments are complex, involving interactions between numerous hydrological components such as soil, bedrock, topography, vegetation cover, and atmosphere (Wigmosta et al., 1994). Aspects of forest management, such as forest structure control or soil conservation, are potentially useful to optimize water yield from headwater catchments (Andréassian, 2004; Grant et al., 2013; Zhang et al., 2016). Physically based, distributed hydrology–vegetation models are promising tools to understand such complex systems and to establish improved protocols for sustainable supply of mountain water to lowlands (e.g. Bahremand, 2016; Moreno et al., 2016).

Interest in the contribution of deep bedrock moisture dynamics to the total water yield from headwater catchments, the focus of this study, has recently increased (Rempe and Dietrich, 2018). Previous studies established that bedrock groundwater predominantly determines the baseflow amount and characteristics (Burns et al., 1998; Fujimoto et al., 2016; Somers and McKenzie, 2020), while others measured a substantial contribution of bedrock groundwater to storm–runoff processes (Iwasaki et al., 2015; Padilla et al., 2015). Additionally, the bedrock groundwater catchment area, inconsistent with the surface catchment area, depends on the intercatchment groundwater flow; thus, it is strongly correlated with the baseflow (Masaoka et al., 2021). Although such publications demonstrated the importance of bedrock hydrology for headwater

* Corresponding author at: Department of Forest Science, Graduate School of Agricultural and Life Sciences, The University of Tokyo, 1-1-1 Yayoi, Bunkyo-ku, Tokyo 113-8657, Japan.
E-mail address: kameyama.toshiaki@gmail.com (T. Kameyama).

https://doi.org/10.1016/j.jhydrol.2025.134205
Received 14 February 2025; Received in revised form 18 August 2025; Accepted 1 September 2025
Available online 4 September 2025

catchments, the dynamics of bedrock groundwater flows remain poorly characterized in entirely physically correct runoff generation models.

Hillslope-scale irrigation experiments demonstrated the connection between rainwater input to soil surface and infiltration into bedrock via soil water movement (e.g. Tromp-van Meerveld et al., 2007). Observations also revealed that bedrock infiltration was controlled by soil moisture at the soil–bedrock interface and could occur in both saturated and unsaturated conditions (Gabrielli and McDonnell, 2018; Kosugi et al., 2006). Moreover, bedrock infiltration and exfiltration, connected with both saturated and unsaturated flow within the bedrock (Katsura et al., 2006; Kosugi et al., 2006), by influencing soil moisture status in the soil layer immediately above the bedrock, resulted in a saturated lateral soil water flow over the bedrock (Katsura et al., 2008; Kosugi et al., 2008). These comprehensive field investigations suggest that coupled bedrock and soil hydrology is a critical requirement for accurate catchment-scale water balance modeling.

Specifically, neglecting bedrock groundwater flow in a hydrologic model induces an overestimation of runoff and evapotranspiration, because groundwater intercatchment flow and discharge through the bedrock are not considered (Staudinger et al., 2019; Tromp-van Meerveld and Weiler, 2008). In this context, the few studies that investigated the influence of bedrock groundwater on catchment runoff with coupled surface water–groundwater models (e.g. Voeckler et al., 2014) could not satisfactorily reproduce measured data (e.g., stream hydrographs, evapotranspiration temporal variations, and spatial distributions of soil moisture and groundwater table), illustrating the necessity of integrated data collection for model calibration and parameterization (Rempe and Dietrich, 2018; Semenova and Beven, 2015). As emphasized in Ala-aho et al. (2017), calibration and optimization of hydrological dynamics parameters in catchment-scale soil–bedrock models require complex algorithms to obtain, simultaneously, realistic estimates of catchment runoff and of the spatial variations of hydrological variables, such as soil moisture or groundwater table depth. This complicates the application of coupled surface water–groundwater models, which is the purpose of this study.

Our objective is to establish a physically based hydrological model with a comprehensive coupled bedrock–soil–vegetation–atmosphere scheme to investigate water resource management and propose improvement strategies. For this purpose, we first develop a distributed hydrological model by aggregating soil and bedrock elementary blocks and simulating their water balance with the Buckingham–Darcy law. Then, applying Bayesian inference to detailed catchment hydrology observations conducted over 8 years, we calibrate the model to optimize the parameters for the observed catchment and to evaluate their uncertainties. Finally, we assess model performance by demonstrating its reproducibility and the importance of bedrock groundwater for catchment runoff generation.

2. Theory and calculation

To describe catchment-scale runoff generation and spatiotemporal soil moisture variations, several scientific teams have developed distributed hydrological models, which consist in aggregating identical elementary soil blocks in which water storage and exchange with adjacent blocks are calculated using standard soil physics principles, such as the Buckingham–Darcy law (Kubota et al., 1988, 1987; Kubota and Sivapalan, 1995; Seibert et al., 2011; Wigmosta et al., 1994). In these distributed models, the effects of topography and of spatial differences in soil depth and properties on catchment hydrological dynamics are evaluated at fine spatial and temporal resolutions with low computational cost. Adding bedrock elementary blocks, we constructed a new, extended distributed hydrological model, the BLock Aggregation of Darcy's law Elements (BLADE) model, to describe the role of bedrock groundwater in generating catchment runoff (Fig. 1). BLADE consists of three submodels that simulate (1) water balance in soil blocks, (2) evapotranspiration from the surface of a soil block, including vegetation, and (3) water balance in bedrock blocks (Fig. 1a). For the simulations, the catchment surface area is divided into equal-size squares cells, each corresponding to one soil and one bedrock block (Fig. 1b). Model equations are solved at each block. Parameters used in this study (symbols, units, and definitions) are listed in Appendix A.

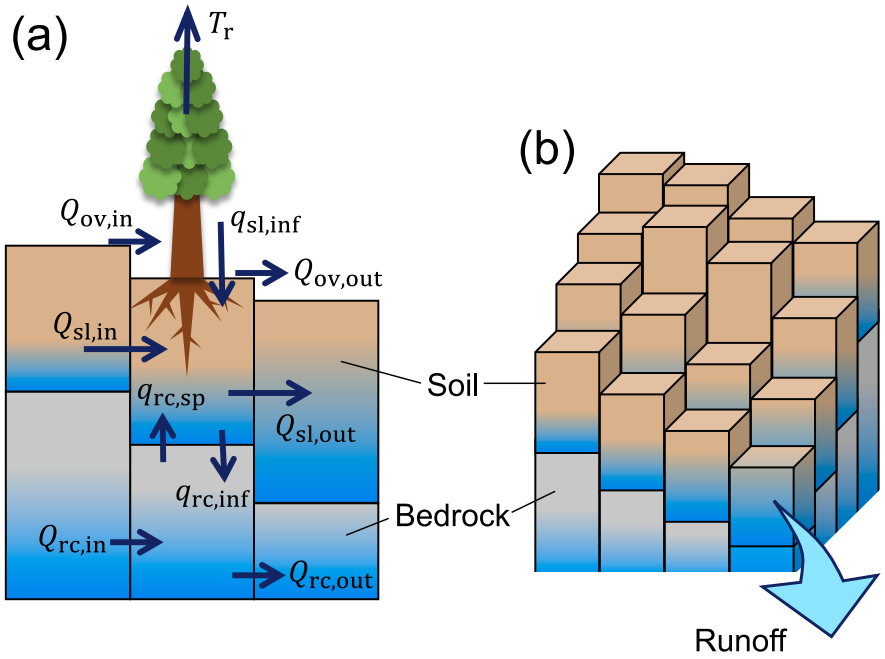

Fig. 1. Schematic illustration of the BLADE model. (a) Water balance in a soil block and in the underlying bedrock block. The contributing water flow rates are T_r: transpiration rate (m h^{-1}); $q_{sl,inf}$: infiltration rate at the soil surface (m h^{-1}); $Q_{ov,in}$ and $Q_{ov,out}$: overland water inflow and outflow rates, respectively (m h^{-1}); $Q_{sl,in}$, $Q_{sl,out}$: lateral water inflow and outflow rates in a soil block, respectively (m^3 h^{-1}); $q_{rc,inf}$, $q_{rc,sp}$: vertical water downward flow (infiltration) and upward flow (spring) rates at the soil–bedrock interface, respectively (m h^{-1}); and $Q_{rc,in}$, $Q_{rc,out}$: lateral inflow and outflow rates in a bedrock block, respectively (m^3 h^{-1}). (b) Model geometry, consisting of two layers (soil and bedrock) of aggregated blocks to represent the catchment.

2.1. Soil hydrology model

We describe the water balance in a soil block (Fig. 1a) with a vertically integrated continuity equation to calculate the mean soil volumetric water content Θ ($m^3\ m^{-3}$):

$$DL^2\frac{\partial\Theta}{\partial t} = L^2\left(q_{sl,inf} - T_r - q_{rc,inf} + q_{rc,sp}\right) + Q_{sl,in} - Q_{sl,out}, \quad (1)$$

where D and L (both in m) are the soil block height and horizontal length, respectively; t is time (h), discretized in the model into time steps separated by a constant time interval Δt; T_r is the vegetation transpiration rate ($m\ h^{-1}$; Section 2.2); q parameters represent vertical water flow rates ($m\ h^{-1}$), with subscripts "sl" and "rc" indicating the soil surface (atmosphere–soil interface) and the soil–bedrock interface, respectively, and subscripts "inf" and "sp" indicating infiltration (downward flow) or spring (upward flow), respectively; and Q_{sl} parameters represent lateral soil water flows ($m^3\ h^{-1}$), with subscripts "in" and "out" indicating inflow and outflow, respectively.

The infiltration rate from the surface into the soil block $q_{sl,inf}$ is expressed as

$$q_{sl,inf} = \begin{cases} P_e + Q_{ov,in} & \text{for } P_e + Q_{ov,in} \le SIC, \\ SIC & \text{for } P_e + Q_{ov,in} > SIC, \end{cases} \quad (2)$$

where P_e is the effective rainfall rate ($m\ h^{-1}$), calculated by subtracting canopy interception from the gross rainfall rate (Section 2.2); $Q_{ov,in}$ is the lateral overland water inflow ($m\ h^{-1}$); and SIC is the soil infiltration capacity ($m\ h^{-1}$) (Philip, 1957a, 1957b), defined as

$$SIC = K_{sat} + \frac{S_p}{2\sqrt{t_p}}, \quad (3)$$

where K_{sat} is the saturated hydraulic conductivity ($m\ h^{-1}$); S_p is the sorptivity (here, 0.035 $m\ h^{-0.5}$ (Talsma, 1969)); and t_p is the sorption duration (h), set to Δt if $P_e + Q_{ov,in} \le SIC$ and to $t_p + \Delta t$ if $P_e + Q_{ov,in} > SIC$.

Based on the Manning formula and plausible hydraulic conditions for mountainous forested streams (David et al., 2010), estimated travel times from the headwaters to the catchment outlet are generally shorter than the model time step ($\Delta t = 1$ h) in the studied catchment. Therefore, we assume that all lateral surface and channel flows can reach the outlet within a single time step. Then, the lateral overland outflow $Q_{ov,out}$ at the surface of a soil block can be expressed as follows:

$$Q_{ov,out} = Q_{Hort} + Q_{ret}, \quad (4)$$

where Q_{Hort} and Q_{ret} are the Hortonian and return overland flows ($m\ h^{-1}$), respectively, with

$$Q_{Hort} = \begin{cases} 0 & \text{for } P_e + Q_{ov,in} \le SIC, \\ P_e + Q_{ov,in} - SIC & \text{for } P_e + Q_{ov,in} > SIC, \end{cases} \quad (5)$$

and

$$Q_{ret} = \begin{cases} 0 & \text{for } \Theta \le \theta_s, \\ \dfrac{(\Theta - \theta_s)D}{\Delta t} & \text{for } \Theta > \theta_s, \end{cases} \quad (6)$$

where θ_s is the soil porosity ($m^3\ m^{-3}$). If $Q_{ret} > 0$, then Θ is adjusted to θ_s. Finally, the inflow $Q_{ov,in}$ over a soil block is equal to the outflow $Q_{ov,out}$ from the adjacent upstream blocks (Fig. 1a and b).

For a downslope water flow q ($m\ h^{-1}$), we approximate ψ at any point within a soil block with the extended Dupuit–Forchheimer assumption (Beven, 1981; Tani, 2008). Because the flow lines are parallel to the soil–bedrock interface, the ψ isocontours are perpendicular (Fig. 2). The hydraulic head is identical at each point of an isocontour and therefore

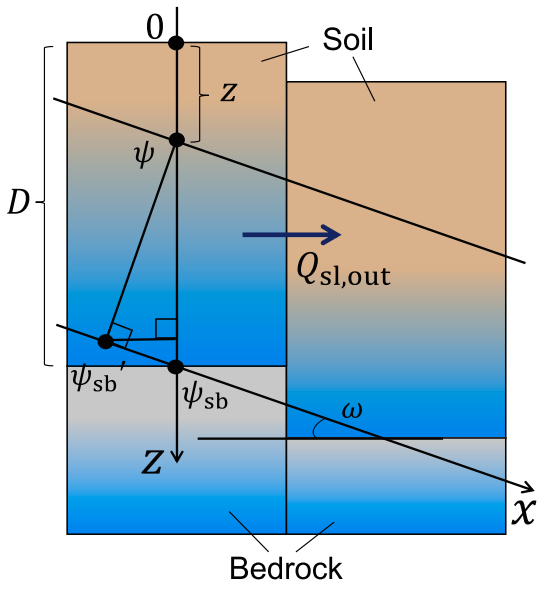

Fig. 2. Schematic illustration of the pressure heads in a soil block. Model parameters are z: depth (m) from the ground surface; x: position (m) along the slope (positive downslope); D: soil block height (m); ψ: soil water pressure head (m); ψ_{sb} and ψ_{sb}': water pressure head (m) at the soil–bedrock interface and at another position along the same isoline, respectively (the position corresponding to ψ_{sb}' is defined in the figure); $Q_{sl,out}$: lateral soil water outflow rate ($m^3\ h^{-1}$); and ω: local slope of the soil–bedrock interface.

$$\psi + (D - z) = \psi_{sb}' + \left[(D - z) - (D - z)\cos^2\omega\right], \quad (7)$$

where ψ is the water pressure head (m) at depth z within the soil block; ψ_{sb} and ψ_{sb}' are water pressure head (m) at the soil–bedrock interface and at another position along the same isoline (Fig. 2), respectively; z is the depth (m), counted positively from the surface; and ω is the local slope of the soil–bedrock interface. Then, considering that $\psi_{sb}' = \psi_{sb}$, the geometric configuration (Fig. 2) yields

$$\psi = \psi_{sb} - (D - z)\cos^2\omega. \quad (8)$$

We further assume that q is governed by a one-dimensional Buckingham–Darcy equation:

$$q = -K\frac{\partial(\psi - x\sin\omega)}{\partial x} = K\left(\sin\omega - \frac{\partial\psi}{\partial x}\right), \quad (9)$$

where x is the position (m) along the contour (positive in the downslope direction; Fig. 2).

Here, we use the Brooks and Corey formulation (Brooks and Corey, 1964) to describe the soil water retention characteristics:

$$S_e = \begin{cases} \left(\dfrac{\psi}{\psi_{ae}}\right)^{-\frac{1}{b}} & \text{for } \psi \le \psi_{ae}, \\ 1 & \text{for } \psi_{ae} < \psi, \end{cases} \quad (10)$$

where S_e is the effective soil saturation; and b is a pore size distribution index.

S_e is expressed as $S_e = (\theta - \theta_r)/(\theta_s - \theta_r)$, with θ and θ_r representing the volumetric water content and the residual volumetric water content (both $m^3\ m^{-3}$), respectively. The corresponding hydraulic conductivity K ($m\ h^{-1}$) is also described using the Brooks and Corey formulation (Brooks and Corey, 1964):

$$K = \begin{cases} K_{sat}S_e^{\,c} & \text{for } \psi \le \psi_{ae}, \\ K_{sat} & \text{for } \psi_{ae} < \psi, \end{cases} \quad (11)$$

where $c = 2b + 3$ is a pore disconnectedness index.

Combining Eqs. (9)–(11), we express the lateral water outflow from a soil block as

$$Q_{sl,out} = W\int_0^D q\cos\omega dz = W\cos\omega \left[\int_0^{z_{ae}} K_{sat}\left(\frac{\psi}{\psi_{ae}}\right)^{-\frac{2b+3}{b}}\left(\sin\omega - \frac{\partial\psi}{\partial x}\right)dz + \int_{z_{ae}}^D K_{sat}\left(\sin\omega - \frac{\partial\psi}{\partial x}\right)dz\right], \tag{12}$$

where W is the width (m) of the block cross-section normal to the water flow direction; and z_{ae} is the depth at air entry water pressure head ψ_{ae} (m). Then, by substituting into Eq. (12) the definition of ψ given in Eq. (8) and by approximating $\partial\psi/\partial x$ as $\partial\psi/\partial x = (\Psi_2 - \Psi_1)\cos\omega/l$, we derive:

$$Q_{sl,out} = W\cos\omega\left(\sin\omega - \cos\omega\frac{\Psi_2 - \Psi_1}{l}\right)\left[\int_0^{z_{ae}} K_{sat}\left\{\frac{\psi_{sb} - (D-z)\cos^2\omega}{\psi_{ae}}\right\}^{-\frac{2b+3}{b}} dz + (D - z_{ae})K_{sat}\right], \tag{13}$$

where Ψ is the soil block mean water pressure head (m), with subscripts 1 and 2 indicating the values in the analyzed block and the adjacent downstream block, respectively; and l is the horizontal distance (m) from the center of a soil block to the center of the adjacent downstream block, i.e., equal to L in the orthogonal direction and to $L\sqrt{2}$ in the diagonal direction. In Eq. (13), z_{ae} is expressed as

$$z_{ae} = D - \frac{\psi_{sb} - \psi_{ae}}{\cos^2\omega}, \tag{14}$$

which is derived by defining $\psi = \psi_{ae}$ at $z = z_{ae}$ in Eq. (8).

We adopt a multiple flow direction algorithm (Quinn et al., 1991) to determine the W values. Calculation of Ψ in the soil block relies on the calculated Θ and the water retention characteristics, described in Eq. (10).

The value of Θ in a specific time step is calculated from Eq. (1) by substituting the terms with their expressions in Eqs. (2)–(10) and with ψ_{sb} set to its value in the previous time step. As in Eq. (13), using the extended Dupuit–Forchheimer assumption (Beven, 1981; Tani, 2008), Eqs. (8) and (10), we express the mean soil volumetric water content in a soil block, $D\Theta$ (m), as:

$$D\Theta = \int_0^D \theta dz = \int_0^{z_{ae}} \left\{(\theta_s - \theta_r)\left[\frac{\psi_{sb} - (D-z)\cos^2\omega}{\psi_{ae}}\right]^{-\frac{1}{b}} + \theta_r\right\}dz + \int_{z_{ae}}^D \theta_s dz. \tag{15}$$

In turn, ψ_{sb} in the specific time step is derived from the calculated Θ with the following equation, derived by Eq. (15):

$$D\Theta = (\theta_s - \theta_r)\int_0^{z_{ae}} \left\{\frac{\psi_{sb} - (D-z)\cos^2\omega}{\psi_{ae}}\right\}^{-\frac{1}{b}} dz + (D - z_{ae})\theta_s + z_{ae}\theta_r. \tag{16}$$

2.2. Evapotranspiration model

In this study, an evapotranspiration model is coupled with the soil hydrology model described in Section 2.1. It comprises the submodels for T_r and for the canopy interception rate I_c (m h^{-1}) designed by Momiyama et al. (2019) and Egusa et al. (2021). Following the study of Kumagai et al. (2014), we estimate I_c from the hourly gross rainfall rate P_g (m h^{-1}) and the interception ratio (r_{IC}):

$$I_c = r_{IC}P_g. \tag{17}$$

Moreover, as indicated in Section 2.1, the effective rainfall rate P_e used in Eq. (2) is defined as $P_e = P_g - I_c$. Although possible r_{IC} estimates vary over a wide range, its exact value does not have a notable impact on the runoff estimation performance (Momiyama et al., 2023). In this study, we set r_{IC} to 0.15 on the basis of the vegetation properties in the study area: canopy type, interception ratio, and occupied area.

For simplicity, we assume that the primary forcing variable for T_r in Japanese plantations is radiative energy (Kumagai et al., 2008). Therefore, BLADE implements a modified version of the expression established by Priestley and Taylor (Priestley and Taylor, 1972) to calculate T_r:

$$T_r = 3600 \times \alpha\frac{\delta}{\rho_w\lambda(\delta + \gamma)}R_n, \tag{18}$$

where α is the Priestley–Taylor coefficient; δ is the slope of the saturation water vapor pressure curve (Pa K^{-1}), which depends on the daily mean air temperature; ρ_w is the water density (kg m^{-3}); λ is the latent heat of water vaporization (here, 2.4×10^6 J kg^{-1}); γ is the psychrometric constant (here, 62 Pa K^{-1}, derived from the mean air pressure at the mean altitude of the studied catchment); and R_n is the net radiation at the canopy top (W m^{-2}). A major factor of uncertainty in Eq. (18) is α, whose value is frequently less than the typical value of 1.26 for forest transpiration, because of additional aerodynamic and canopy resistance (Kumagai et al., 2004). Here, we calculate monthly α values from Eq. (18) for the simulation period using monthly mean R_n and transpiration data. Transpiration data are estimated by subtracting canopy interception from evapotranspiration, itself derived for the entire catchment with the short-term water budget method (Momiyama et al., 2019). The resulting maximum and minimum α values are 0.679 in November and 0.0519 in April, respectively.

2.3. Bedrock hydrology model

We also describe the water balance in a bedrock block (Fig. 1a) adjacent to the analyzed soil block with a vertically integrated continuity equation to calculate the groundwater table depth z_{gw} (m):

$$\phi_{rc}\frac{\partial z_{gw}}{\partial t} = \frac{1}{L^2}\left(Q_{rc,out} - Q_{rc,in}\right) - q_{rc,inf}, \tag{19}$$

where ϕ_{rc} is the bedrock porosity (m^3 m^{-3}); and $Q_{rc,in}$ and $Q_{rc,out}$ are the lateral bedrock water inflow and outflow (m^3 h^{-1}), respectively. The control exerted by soil moisture conditions on $q_{rc,inf}$ (Gabrielli and McDonnell, 2018; Katsura et al., 2006; Kosugi et al., 2006) is functionally expressed as:

$$q_{rc,inf} = \begin{cases} K_{rc,vsat}\left(\frac{\psi_{sb}}{\psi_{ae}}\right)^{-\frac{2b+3}{b}} & \text{for } z_{gw} > D \text{ and } \psi_{sb} \le \psi_{ae}, \\ K_{rc,vsat} & \text{for } z_{gw} > D \text{ and } \psi_{ae} < \psi_{sb}, \\ 0 & \text{for } z_{gw} \le D, \end{cases} \tag{20}$$

where $K_{rc,vsat}$ is the saturated bedrock hydraulic conductivity (m h^{-1}) for vertical flow. Here, ψ_{sb} is the critical variable; therefore, its prior calculation with the soil hydrology model is essential to solve Eq. (19), which calculation implies, if $z_{gw} < D$, that $q_{rc,sp}$ in Eq. (1) is expressed as

$$q_{rc,sp} = \frac{\phi_{rc}(D - z_{gw})}{\Delta t}, \tag{21}$$

and z_{gw} is adjusted to D.

In the BLADE bedrock hydrology submodel, we assume anisotropic hydraulic conductivity and express the saturated bedrock hydraulic conductivity for lateral flow (m h^{-1}), following Beven and Kirkby (1979), as

$$K_{\mathrm{rc,lsat}}(z) = K_{\mathrm{rc,lsat\_0}}\exp[-f_{\mathrm{rc}}(z-D)], \tag{22}$$

where $K_{\mathrm{rc,lsat\_0}}$ is the value in the topmost bedrock region (near the soil–bedrock interface); and f_{rc} (m^{-1}) is an attenuation factor defining the dependence of $K_{\mathrm{rc,lsat}}$ on depth z. Consequently, Q_{rc} is expressed as:

$$\begin{aligned} Q_{\mathrm{rc,out}} &= W\cos\omega_{\mathrm{gw}}\int_{z_{\mathrm{gw}}}^{\infty} K_{\mathrm{rc,lsat}}\sin\omega_{\mathrm{gw}}\,dz \\ &= W\cos\omega_{\mathrm{gw}}\sin\omega_{\mathrm{gw}}\frac{K_{\mathrm{rc,lsat\_0}}}{f_{\mathrm{rc}}}\exp[-f_{\mathrm{rc}}(z_{\mathrm{gw}}-D)], \end{aligned} \tag{23}$$

where ω_{gw} is the local slope of the groundwater table; and $-\sin(\omega_{\mathrm{gw}})$ is the hydraulic gradient. The inflow $Q_{\mathrm{rc,in}}$ is equal to the outflow $Q_{\mathrm{rc,out}}$ from the adjacent upstream bedrock block. Finally, we assume an absence of lateral bedrock flow between the outside region and the studied catchment, i.e., $Q_{\mathrm{rc,in}} = 0$ at the upstream boundary and $Q_{\mathrm{rc,out}} = 0$ below the catchment outlet (Oda et al., 2013).

3. Methodology

3.1. Study area

For this study, we selected the Oborasawa Experimental Watershed (OEW), a forest headwater catchment with an area of 49 ha (35°28′N, 139°12′E; Fig. 3) located in the Tanzawa mountains of the Kanto region, Japan. The catchment is steep and covers an altitude range of 439–872 m, with a slope of 37.1° ± 8.5° (mean ± standard deviation). The mean annual precipitation for 2010–2017 was 2954 mm. The soil, classified as Cambisol, contains abundant volcanic ash and is largely homogeneous across the catchment; its surface infiltration capacity is high, within 100–600 mm h^{-1} (Oda et al., 2013). The underlying tuff bedrock, composed mainly of volcanic breccia, is classified as Cenozoic sedimentary rock and is similarly homogeneous. A previous study, using the chloride mass balance method, indicated a negligible annual inter-catchment groundwater flow in the studied catchment, of approximately 5 % of the annual runoff (Oda et al., 2013).

The OEW is heavily forested, with a proportion of bare land of less than 1 %. Vegetation consists primarily of coniferous plantation stands covering approximately two thirds of the forested areas, planted mainly with *Cryptomeria japonica* D. Don and a smaller proportion of *Chamaecyparis obtusa* Endl. The remaining forest is fragmented into smaller patches of deciduous broadleaved trees, such as *Cercidiphyllum japonicum* Sieb. et Zucc., *Aesculus turbinata* Blume, and *Fraxinus spaethiana* Lingelsh. The estimated mean stem density and plant area index for the catchment are 1280 trees ha^{-1} and 3.8 m^2 m^{-2}, respectively.

3.2. Study data

We acquired meteorology, rainfall–runoff, soil moisture, bedrock groundwater table, and vegetation throughfall and stemflow data, well suited for BLADE validation, for the study area in 2010–2017. Locations of the instruments and observation sites are reported in Fig. 3.

Meteorological data were acquired every 10 min, primarily at the weather station on the open ridge of the catchment (eastern catchment boundary, Fig. 3). Solar radiation was measured with a pyranometer (SL-30, Azbil, Tokyo, Japan); the net radiation R_{n} used in Eq. (18) was then derived by scaling the solar radiation by a factor of 0.8 (Komatsu et al., 2007). Air temperature and relative humidity were measured with a relative humidity probe (HT-20, Azbil, Tokyo, Japan). Finally, rainfall was measured with two 0.5-mm tipping-bucket rain gauges (N78, Nippon Electric Instrument, Tokyo, Japan) at two locations: the open-ridge weather station and near a V-notch weir placed at the lowest point of the catchment stream (northeastern catchment boundary; Fig. 3). Measurements, calibration, and correction of these data have been reported in a previous publication (Egusa et al., 2021) and will not be detailed here.

From these measurements, we derived an annual mean air temperature of 13.4 °C, with a minimum daily mean value of −3.6 °C in February and a maximum daily mean value of 30.3 °C in August. We averaged the very consistent rainfall values, measured at both observation points, to represent the mean rainfall in the catchment and derived a mean annual rainfall of 2954 mm. Large rainfall events generally occurred during the rainy season from mid-June to early July (mean ± standard deviation: 584 ± 206 mm) and during the typhoon season in September–October (921 ± 235 mm). Snowfall occurred once or twice yearly between January and March, but represented only a small percentage of the total annual precipitation, with limited influence on runoff.

A pressure-type water level gauge (ATM_N, Koshin Denki, Tokyo, Japan) installed on the V-notch weir provided stream water level data

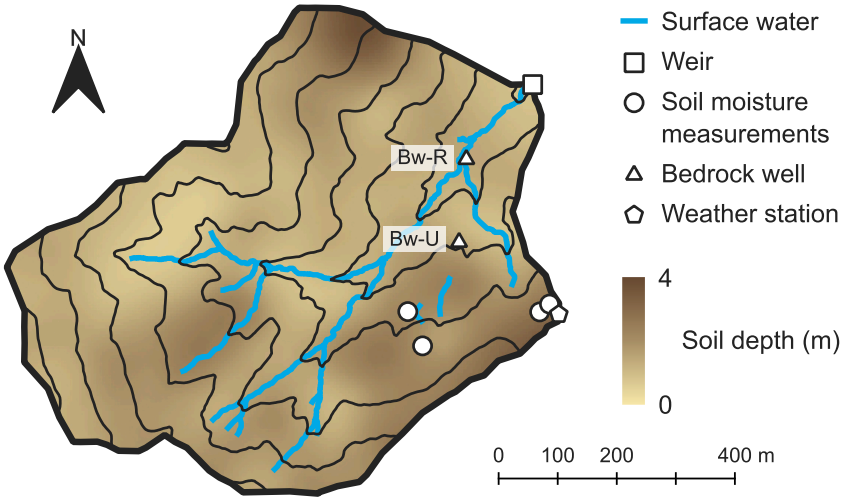

Fig. 3. Map of the study area. The 49-ha experimental catchment is dedicated to water budget observations. Topography is superimposed on a soil depth map, with altitude isocontours every 50 m between 450 m (northeast near the weir) and 850 m (southwest). The horizontal scale is also indicated. White symbols indicate measurement sites. The two bedrock wells are labeled BW-R (riparian zone, downslope) and BW-U (upslope).

(also every 10 min) that we converted to volumetric runoff through the empirical relationship established in Egusa et al. (2021). Then, we divided the volumetric runoff by the contributing catchment area to derive the specific discharge (hereinafter "runoff").

Soil depth, measured by cone penetration, was 1.59 ± 0.97 m (mean ± standard deviation; $n = 170$; Fig. 3). The soil volumetric water content and water pressure head were measured regularly during part of the study period at four locations (Fig. 3) and at depths of 10 cm, 30 cm, and 70 cm below the forest floor. For the volumetric water content, we used a time domain reflectometer (CS616, Campbell Scientific, Logan, Utah, USA). For the water pressure head, we used a specially ordered tensiometer (Environmental Measurement Japan Co. Ltd., Fukuoka, Japan). By operating both instruments at the same depths, we were able to obtain in situ soil water retention curves. Moreover, we collected soil core samples near the soil moisture measurement sites and analyzed them with the steady-state infiltration method (DIK-4011, Daiki Rika Kogyo Co., Ltd., Saitama, Japan) to derive the saturated hydraulic conductivity in the upper soil layers. Finally, because of the large variation range of hydraulic conductivity values, we calculated its geometric mean and obtained a value of 0.527 m h^{-1}.

In the OEW catchment area, weathered and fissured bedrock has been identified at depths of 40 m or more below the soil surface (Yokoyama et al., 2013). Thus, two 50-m-deep bedrock wells, labeled BW-R (riparian zone, downslope) and BW-U (upslope) in Fig. 3, were dug at altitudes of 479.2 m and 547.3 m (Fig. 3) to monitor the groundwater table depth during the study period. In each well, which did not allow inflow from above the bedrock, the groundwater head was measured with a pressure-type water level gauge (UIZ-WL1000-N19-15; Uizin, Tokyo, Japan). Additionally, the bedrock saturated hydraulic conductivity for lateral flow was measured with a drill stem test (Johnston's formation test; Japanese Geotechnical Society, 2003) at depths of 20.5 m, 26.5 m, 38.5 m, and 44.5 m in the riparian zone (downslope) well and 22.0 m, 29.5 m, 36.5 m, and 46.5 m in the upslope well. The resulting values, depending on the degree of weathering, were within 9.18×10^{-5}–1.68×10^{-3} m h^{-1} and 6.05×10^{-4}–2.68×10^{-3} m h^{-1} at the riparian zone and upslope wells, respectively (Yokoyama et al., 2013).

Finally, for this study, we selected four plots representative of the vegetation types in the study area for throughfall and stemflow measurements: a *Cr. japonica* plot, a *Ch. obtusa* plot, and two mixed hardwood tree plots comprising *Ce. japonicum*, *A. turbinata*, and *F. spaethiana*. Throughfall was measured with collectors randomly dispersed over each plot: 14–18 for *Cr. japonica*, 7–11 for *Ch. obtusa*, and 10 for each hardwood tree plot. The collectors included manually operated gauges assembled from plastic funnels (diameter: 21 cm) and plastic bottles (capacity: 10 L or 20 L). For stemflow measurements, collars placed around tree trunks to catch the stemflow were connected to plastic bottles (capacity: 50 L or 70 L); tipping-bucket flowmeters (volume: 0.2 or 0.5 L) were used on five trees in the *Cr. japonica* plot, four trees in the *Ch. obtusa* plot, and five trees in one hardwood tree plot. Interception ratios derived from these measurements were for 14.8 % and 20.6 % for *Cr. japonica* and *Ch. obtusa*, respectively, using data acquired in 2019, and 12.0 % for the hardwood trees, using 2009–2010 data.

3.3. Numerical simulations

To analyze the contribution of bedrock water flow dynamics to the rainfall–runoff process during the study period, we designed two BLADE versions: one restricted to soil blocks (BL-S) and one including both soil and bedrock blocks, i.e., the full BLADE model (BL-S&B). We compared their prediction performance and the simulated rainfall–runoff process. We calibrated both models by applying Bayesian inference to prior distributions of nine parameters aggregated into a parameter vector $\mathbb{X}$: θ_s, θ_r, ψ_{ae}, b, K_{sat}, ϕ_{rc}, $K_{rc,vsat}$, $K_{rc,lsat\_0}$, and f_{rc} (Table 1), to evaluate model fitness and optimize $\mathbb{X}$ for each model.

For the simulations, we set the spatial and temporal resolutions to $L = 5$ m and $\Delta t = 1$ h, respectively. We used the 2010 data for model initialization (spin-up) to determine the initial values of S_e and z_{gw}. Then, we compared the modeled runoff Q at the catchment outlet over the remaining 7-year observation period (2011–2017) and applied the Nash–Sutcliffe efficiency (NSE) criterion (Nash and Sutcliffe, 1970) to evaluate parameter optimization and model fitness under three hydrological regimes (Criss and Winston, 2008; Krause et al., 2005; Pushpalatha et al., 2012). High, low, and balanced streamflow conditions were evaluated with the ordinary NSE (NSE_o), NSE with inverse Q values (NSE_{inv}), and NSE with the natural logarithm of Q values (NSE_{ln}), respectively, expressed as:

$$NSE_o = 1 - \frac{\sum_{i=1}^{N}(Q_{oi} - Q_{mi})^2}{\sum_{i=1}^{N}(Q_{oi} - \overline{Q_{oi}})^2}, \tag{24}$$

$$NSE_{inv} = 1 - \frac{\sum_{i=1}^{N}\left(\frac{1}{Q_{oi}+\varepsilon} - \frac{1}{Q_{mi}+\varepsilon}\right)^2}{\sum_{i=1}^{N}\left\{\frac{1}{Q_{oi}+\varepsilon} - \overline{\left(\frac{1}{Q_{oi}+\varepsilon}\right)}\right\}^2}, \tag{25}$$

and

$$NSE_{ln} = 1 - \frac{\sum_{i=1}^{N}\{\ln(Q_{oi}+\varepsilon) - \ln(Q_{mi}+\varepsilon)\}^2}{\sum_{i=1}^{N}\{\ln(Q_{oi}+\varepsilon) - \overline{\ln(Q_{oi}+\varepsilon)}\}^2}, \tag{26}$$

where i is a time step index varying from 1 to the total number of time steps, N; subscripts "o" and "m" represent the observed and simulated runoff values, respectively; the overbar indicates ensemble mean values; and ε is the zero-runoff displacement (Pushpalatha et al., 2012). We excluded winter Q values (January–March) from NSE calculations to avoid snowfall and snowmelt effects.

Table 1
Prior distributions of parameter values used for BLADE calibration.

Parameter*1	Unit	Range		Definition
		Minimum	Maximum	
θ_s	$m^3\ m^{-3}$	0.3	0.7	Soil porosity
θ_r	$m^3\ m^{-3}$	0.05	0.2	Residual soil volumetric water content
ψ_{ae}	m	−0.4	−0.05	Air entry water pressure head
b		0.5	3.0	Soil pore size distribution index
K_{sat}*2	m h^{-1}	0.1	2.0	Saturated soil hydraulic conductivity
ϕ_{rc}	$m^3\ m^{-3}$	0.01	0.1	Bedrock porosity
$K_{rc,vsat}$*2	m h^{-1}	10^{-5}	10^{-2}	Saturated bedrock hydraulic conductivity for vertical flow
$K_{rc,lsat\_0}/K_{rc,vsat}$		$10^{-0.5}$	10	Saturated bedrock hydraulic conductivity for lateral flow ($K_{rc,lsat}$) in the topmost bedrock region normalized by $K_{rc,vsat}$
f_{rc}*3	m^{-1}	0.011	0.23	Attenuation factor defining the dependence of $K_{rc,lsat}$ on depth z

*1 Uniform distributions assumed for each parameter, except as described in footnotes *2 and *3.
*2 Prior and posterior distributions derived from the common logarithm of the parameter.
*3 Prior and posterior distributions derived from $\exp(-10 f_{rc})$.

The posterior $\mathbb{X}$ distribution, noted $\pi(\mathbb{X}|\mathrm{NSE})$, was described as:

$$\pi(\mathbb{X}|\mathrm{NSE}) \propto f(\mathrm{NSE}|\mathbb{X})\pi(\mathbb{X}), \tag{27}$$

where $f(\mathrm{NSE}|\mathbb{X})$ is the likelihood; and $\pi(\mathbb{X})$ is the prior $\mathbb{X}$ distribution, assumed uniform (see Table 1 for value ranges) for most parameters except for K_{sat}, $K_{\mathrm{rc,vsat}}$, $K_{\mathrm{rc,lsat\_0}}$, and f_{rc}, for which we used uniform distributions of the common logarithm (K_{sat} and $K_{\mathrm{rc,vsat}}$), the ratio $K_{\mathrm{rc,lsat\_0}}/K_{\mathrm{rc,vsat}}$, and $\exp(-10f_{\mathrm{rc}})$, respectively, to account for their possible range of variation and their anisotropy. We estimated the likelihood, i.e., the NSE probability distribution, by Markov Chain Monte Carlo sampling of $\pi(\mathbb{X})$. In the Metropolis algorithm, we first select a specific sample $\mathbb{X}_j$, representing a parameter vector $\mathbb{X}$ at iteration j, from the original dataset (prior distribution $\pi(\mathbb{X})$). We define $\mathbb{X}_{j+1}$ as

$$\mathbb{X}_{j+1} = \mathbb{X}_j + \Delta X, \tag{28}$$

where $\Delta\mathbb{X}$ is an arbitrary increment, and $\mathbb{X}_{j+1}$ must also be included in the dataset.

Then, we calculate NSE values NSE_j and NSE_{j+1}, calculated with the corresponding vector, which provide a decision criterion for acceptance or rejection of the candidate sample (Eq. (28)):

$$\text{If } \mathrm{NSE}_{j+1} \geq \mathrm{NSE}_j, \text{ then } \mathbb{X}_{j+1} = \mathbb{X}_j + \Delta X. \tag{29}$$

Conversely,

$$\text{If } \mathrm{NSE}_{j+1} < \mathrm{NSE}_j, \text{ then } \mathbb{X}_{j+1} = \begin{cases} \mathbb{X}_j + \Delta\mathbb{X} & \text{adopted with } p_{\mathrm{ac}}, \\ \mathbb{X}_j & \text{adopted with } 1 - p_{\mathrm{ac}}, \end{cases} \tag{30}$$

where p_{ac} is the acceptance probability, defined as $\mathrm{NSE}_{j+1}/\mathrm{NSE}_j$.

Applying this algorithm to a set of 26068 $\mathbb{X}$ samples randomly selected from the original $\pi(\mathbb{X})$ dataset, we calculated Q and NSE for each sample and finally obtained the NSE frequency distribution, with 25000 aggregated NSE samples, enough number for convergence of the posterior $\mathbb{X}$ distribution, and only 1068 pre-convergence samples (burn-in samples), a small but sufficient number, because random sampling rapidly limits the influence of the initial sample parameters.

For quantification, we defined the contribution ratio of bedrock water to surface water (α_{surf}) at time step t at the surface of a soil block:

$$\alpha_{\mathrm{surf}} = \frac{\left(\sum_{\mathrm{up}} \alpha_{\mathrm{surf,in}} Q_{\mathrm{ov,in}} \Big/ \sum_{\mathrm{up}} Q_{\mathrm{ov,in}}\right)^{t-\Delta t} Q_{\mathrm{ov,out}} + \alpha_{\mathrm{soil}} Q_{\mathrm{ret}}}{Q_{\mathrm{ov,out}} + Q_{\mathrm{ret}}}, \tag{31}$$

with

$$\alpha_{\mathrm{soil}} = \frac{\left[DL^2\Theta\alpha_{\mathrm{soil}} + \left\{ \begin{array}{l} \alpha_{\mathrm{surf}} L^2 q_{\mathrm{sl,inf}} + \sum_{\mathrm{up}} \alpha_{\mathrm{soil,in}} Q_{\mathrm{sl,in}} + L^2 q_{\mathrm{rc,sp}} \\ -\alpha_{\mathrm{soil}} \left(\sum_{\mathrm{down}} Q_{\mathrm{sl,out}} + L^2 q_{\mathrm{rc,inf}} + L^2 T_{\mathrm{r}} \right) \end{array} \right\} \Delta t \right]^{t-\Delta t}}{DL^2\Theta}, \tag{32}$$

where α_{soil}, the contribution ratio of the bedrock water to soil water storage at time step t, is derived from the continuity equation of the previous time step $t-\Delta t$, and Σ_{up} and Σ_{down} represent summation of the water flow from upstream blocks and to downstream blocks, respectively. Ultimately, the bedrock water contribution to the total runoff Q is the value of α_{surf} at the catchment outlet and is obtained by sequentially calculating these contributions from the topmost catchment blocks to the outlet.

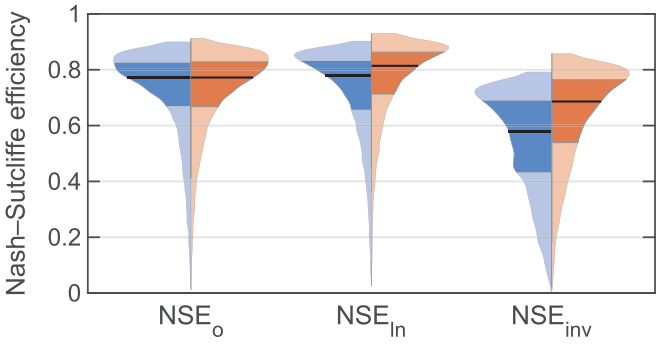

Fig. 4. Comparison of three Nash–Sutcliffe efficiency (NSE) calculations for runoff outputs from the BL-S (blue shading) and BL-S&B (red shading) model versions. The three NSE values comprise $\mathrm{NSE_o}$ (ordinary NSE), $\mathrm{NSE_{ln}}$ (calculated with the natural logarithm of runoff values), and $\mathrm{NSE_{inv}}$ (calculated with inverse runoff values). Probability distributions (violin plot, light shading) were estimated with kernel smoothing density functions. The thick horizontal line and darker shading indicate the median and the interquartile range, respectively. (For interpretation of the references to colour in this figure legend, the reader is referred to the web version of this article.)

4. Results

4.1. Comparison of model parameters for BL-S and BL-S&B

We first compared the three NSE evaluations for runoff output simulated with BL-S and BL-S&B (Fig. 4). Maximum consistency between the models was obtained for $\mathrm{NSE_o}$, with nearly identical median values, whereas the median $\mathrm{NSE_{ln}}$ and $\mathrm{NSE_{inv}}$ values were slightly and markedly higher, respectively, for BL-S&B than for BL-S, indicating that model performance under low-flow conditions clearly improved when bedrock hydrology was included in the simulation.

Posterior probability distributions of the nine model parameters (Fig. 5) were derived for BL-S and BL-S&B, but only for data samples with a calculated $\mathrm{NSE_{inv}}$ exceeding its median value (Fig. 4, right). Because BL-S only includes soil hydrology, model parameters for the soil layer: θ_{s}, θ_{r}, ψ_{ae}, b, and K_{sat} were nearly optimal for accurate runoff simulation, as illustrated by the clear peaks in their probability distributions (Fig. 5, top row). Conversely, BL-S&B also considers bedrock hydrology, yielding probability distributions that remained approximately uniform for soil hydrology parameters (Fig. 5, top row), but nearly optimal for bedrock hydrology parameters ϕ_{rc}, $K_{\mathrm{rc,vsat}}$, $K_{\mathrm{rc,lsat\_0}}$, and f_{rc} (Fig. 5, bottom row). This demonstrates that bedrock hydrology is crucial for realistic mountain hydrology simulations.

Curves for soil water retention (θ–ψ relationship) and for the K–ψ relationship were established for each model using the soil hydrology parameters with calculated $\mathrm{NSE_{inv}}$ values exceeding its median and then compared with the θ–ψ relationship and K_{sat} values effectively observed in the surface soil layer (Fig. 6). Results for soil water retention indicated that BL-S overestimated the effective soil porosity θ_{s}–θ_{r} (Fig. 6a1), whereas BL-S&B results were consistent with the measurements (Fig. 6a2). In addition, BL-S could not reproduce the measured K_{sat} values (Fig. 6b1), whereas the BL-S&B simulated values were reasonably consistent with the measurements (Fig. 6b2). This implies that measuring soil hydrology parameters is not sufficient for accurate catchment water balance simulations if bedrock hydrology is not considered. In fact, adjusting BL-S model parameters to optimize the consistency between model output and measured data might yield unphysical soil hydrology parameter values.

4.2. Reproduction of runoff and bedrock groundwater table depth

On the basis of the results described in Section 4.1, we designed further simulations to evaluate runoff and bedrock groundwater table

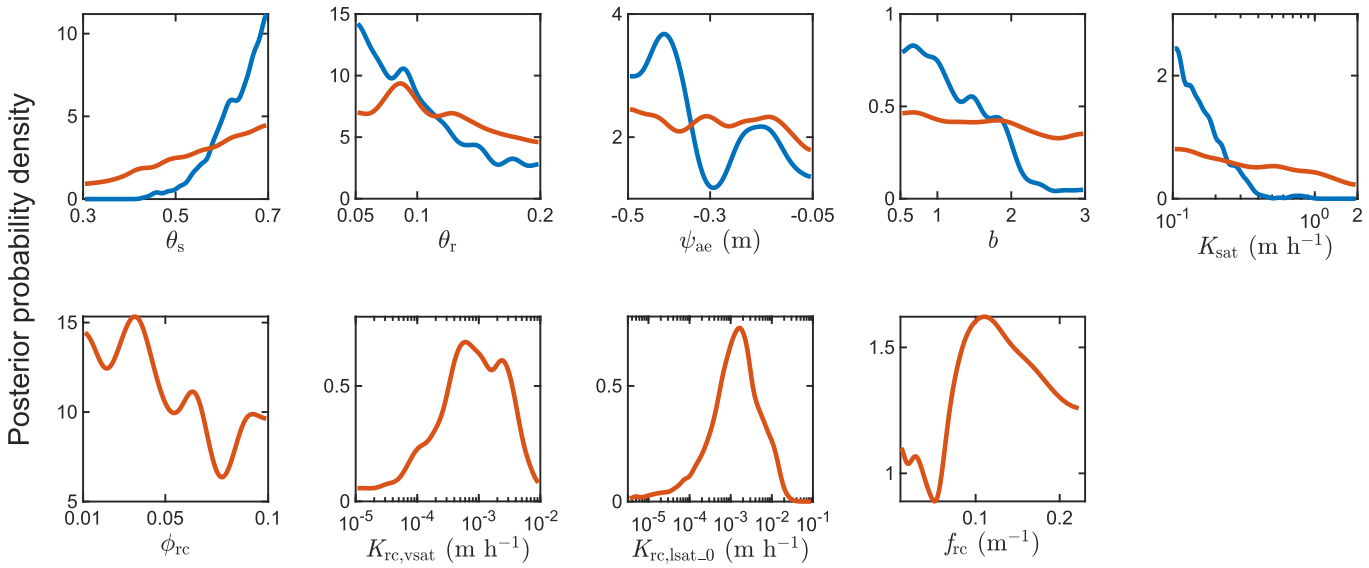

Fig. 5. Posterior probability distributions of the model parameters. See text and Table 1 for calculation, with the parameters: θ_s: soil porosity; θ_r: residual soil volumetric water content; ψ_{ae}: air entry water pressure head; b: soil pore size distribution index; K_{sat}: saturated soil hydraulic conductivity; ϕ_{rc}: bedrock porosity; $K_{rc,vsat}$: saturated bedrock hydraulic conductivity for vertical flow; $K_{rc,lsat\_0}$: saturated bedrock hydraulic conductivity for lateral flow in the topmost bedrock region; and f_{rc}: attenuation factor defining the dependence of $K_{rc,lsat}$ on depth. Distributions were derived using kernel smoothing density functions for both BL-S (blue curves) and BL-S&B (red curves), but only for data samples with NSE_{inv} values exceeding its median (Fig. 4). (For interpretation of the references to colour in this figure legend, the reader is referred to the web version of this article.)

depth with the BL-S&B model version and only for data samples with NSE_{inv} values exceeding its median (Fig. 5). We compared BL-S&B simulation results with the observed hourly variations of the catchment runoff and bedrock groundwater table depth at two locations, in the riparian zone and upslope (Fig. 3). By accounting for snow accumulation and melting, the simulation period extended from 1 April to 31 December 2017 (Fig. 7).

The model reproduced the observed catchment runoff very well (Fig. 7a), clearly indicating that bedrock hydrology parameters contribute more strongly to the simulation performance than soil parameters (see also Fig. 5). The observed variations in the median bedrock groundwater table depth were acceptably traced by BL-S&B in the riparian zone, despite substantial amplitude discrepancies (Fig. 7b). At the upslope location, observed values were only marginally outside the 95 % confidence interval of the simulation (Fig. 7c).

4.3. Relationship between runoff generation and bedrock groundwater flow dynamics

We compared the spatial distribution of the partial catchment area derived from ground surface topography, as represented by a digital elevation model (CA_{top}; Fig. 8a), and from the simulated bedrock groundwater table depth during a large rainfall event (CA_{bg}; Fig. 8b), as well as their cumulative ratios (Fig. 8c). The CA_{top} and CA_{bg} distributions were concentrated within partial catchment area ranges of approximately 3–20 m^2 and 20–40 m^2, respectively, implying that the area contributing to rainwater collection and mixing was substantially broader for bedrock groundwater than for the water flow in the surface soil layer. Comparing the CA_{bg} to CA_{top} ratio over the entire catchment (Fig. 8d), we determined that CA_{top} was larger in the stream channel and the valleys, whereas CA_{bg} dominated in the riparian zone and adjacent slopes. Therefore, we infer that soil water and bedrock groundwater in the riparian and slope zones were generated from a rainwater collection area extending beyond the local scale. Here, to derive the partial catchment area, the multiple flow direction algorithm (Quinn et al., 1991) was adopted for determining the water flow directions.

We also investigated the relationships between simulated infiltration and spring (into and from bedrock, respectively) at the soil–bedrock interface and catchment-mean effective soil saturation defined as $\langle S_e \rangle = \sum D(\Theta - \theta_r) / \sum D(\theta_s - \theta_r)$, where Σ represents summation over the catchment (Fig. 9a). Then, by calculating the spatiotemporal variations of the contribution ratio of bedrock groundwater to surface water and soil water storage (Eqs. (31) and (32)), we inferred the relationship between the contribution ratio of bedrock groundwater to the total catchment runoff and the runoff itself (Fig. 9b). This relationship exhibits a clear hysteresis that we explain as follows: during low-flow periods, when a decrease in Θ and, accordingly, in $\langle S_e \rangle$, reduced infiltration into the bedrock, the spring from the bedrock was larger than the lateral soil water flow (Fig. 9a), resulting in a considerably larger contribution of bedrock groundwater to runoff (Fig. 9b). A consecutive $\langle S_e \rangle$ increase strongly enhanced infiltration into the bedrock, increasing bedrock groundwater storage. Subsequently, bedrock infiltration and storage both saturated, enhancing spring from the bedrock (Fig. 9a). Simultaneously, the direct lateral soil water flow (not passing through the bedrock) contributed substantially to the catchment runoff, reducing the relative contribution of bedrock groundwater (Fig. 9b).

When soil dried after a wet period, $\langle S_e \rangle$ decreased, temporarily causing the bedrock water inflow and outflow to occur at similar rates (catchment-mean effective soil saturation within 0.6–0.65; Fig. 9a). At this time, the relative contribution of bedrock groundwater remained stable, despite a net decrease in the catchment runoff (Fig. 9b). As soil continued to dry, bedrock infiltration substantially decreased, while the bedrock spring rate remained stable (Fig. 9a). This continuous outflow from the bedrock near the stream channel, concurrent with a decrease in the soil water outflow, explains the smaller contribution of soil water to catchment runoff (Fig. 9b).

5. Discussion

5.1. Validity of the BLADE model

Until recently, most studies on coupled surface water–groundwater modeling did not account for bedrock hydrology and considered the soil–bedrock interface as the bottom boundary of the model domain (e.g. Ala-aho et al., 2017; Broda et al., 2011). Kosugi et al. (2011) were among the first to demonstrate the influence of interactions between soil

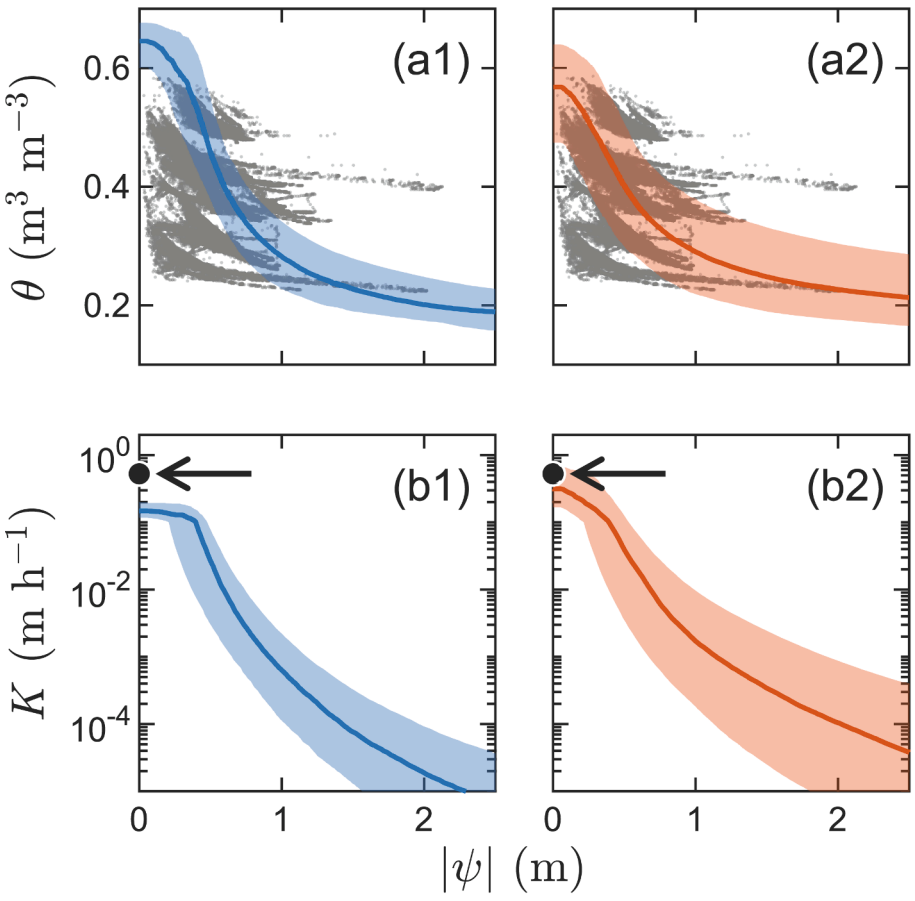

Fig. 6. Dependence of soil water retention and hydraulic conductivity on the pressure head ψ. Soil water retention refers to the relationship between the volumetric water content θ and ψ (Panels a1–a2, top). Hydraulic conductivity K is shown in Panels b1–b2 (bottom). Both relationships were calculated only for data samples with NSE_{inv} values exceeding its median (Fig. 4). Simulation results are represented for BL-S (blue, left) and BL-S&B (red, right) by the median (thick solid curve) and interquartile range (shading). Soil water retention observations (gray dots; Panels a1–a2) and geometric mean of the measured saturated hydraulic conductivity K_{sat} (filled circle with arrow; Panels b1–b2) are also indicated. (For interpretation of the references to colour in this figure legend, the reader is referred to the web version of this article.)

and bedrock hydrological processes on runoff generation, by applying a simple hydrological model to intensive observations from densely located bedrock wells. They achieved reasonable reproduction of the multiple peaks in catchment runoff time series caused by the spatial distribution and temporal evolution of bedrock groundwater. However, their model, unlike BLADE, was mainly conceptual, one-dimensional, and assumed simple storage–runoff models for only three hydrological components: the outflows from soil mantle groundwater and from lower and mid-bedrock aquifers.

However, in the past decade, the possible contribution of bedrock groundwater dynamics to catchment outflow generation has been increasingly considered, notably since the pioneering study of Voeckler et al. (2014), who developed a physically distributed hydrological model in which the bedrock was treated as permeable. Concurrently, other studies developed physically-based hydrological models that explicitly considered hillslope-scale bedrock hydrology (e.g. Ameli et al., 2015; Lanni et al., 2013). More recently, Camporese et al. (2019) analyzed the influence of spatial variations in the water table response at the soil–bedrock interface on the generation of hillslope-scale storm runoff using a physically-based distributed model with detailed bedrock description. The originality of our study is that BLADE is a comprehensive, physically-based, distributed hydrology–vegetation model with soil–bedrock coupling that fully accounts for bedrock water flow.

Arguably, developing coupled surface water–groundwater models is a complex task, not only in terms of mathematical and physical formulation but also of calibration and parameter optimization. Indeed, as summarized in Ala-aho et al. (2017), integrated surface–subsurface models require extensive observation data for simultaneous parameterization and simulation of catchment-scale hydrological processes, which precludes straightforward operational use. Furthermore, direct bedrock hydrology observations, which are necessary to constrain distributed hydrology–vegetation models by accounting for bedrock moisture dynamics, remain scarce (Rempe and Dietrich, 2018). In our study, we were able to validate BLADE by applying innovative parameter optimization methods to extensive, high-quality catchment-scale hydrological observations.

More precisely, implementing physically-based comprehensive hydrological models such as BLADE is extremely challenging because it requires simultaneous reproduction of observed data, e.g., evapotranspiration, soil moisture, and groundwater table depth from diverse hydrological domains (e.g., vegetation, soil surface and mantle, and bedrock) using mechanistic model simulations that include physically meaningful parameters (Ala-aho et al., 2017). This explains the difficulties for numerical processing and the parameterization instabilities of such models that prevent their broader adoption by hydrology scientists worldwide (Hrachowitz and Clark, 2017). Moreover, if reproducing observations from all modeled domains is not required during model parameter calibration, the calibration might implicitly compensate for structural model errors by improving the model fit for the main observation, for example catchment runoff, regardless of the results in other domains (Semenova and Beven, 2015). For example, for rainfall–runoff processes that intrinsically include numerous hydrological domains, the

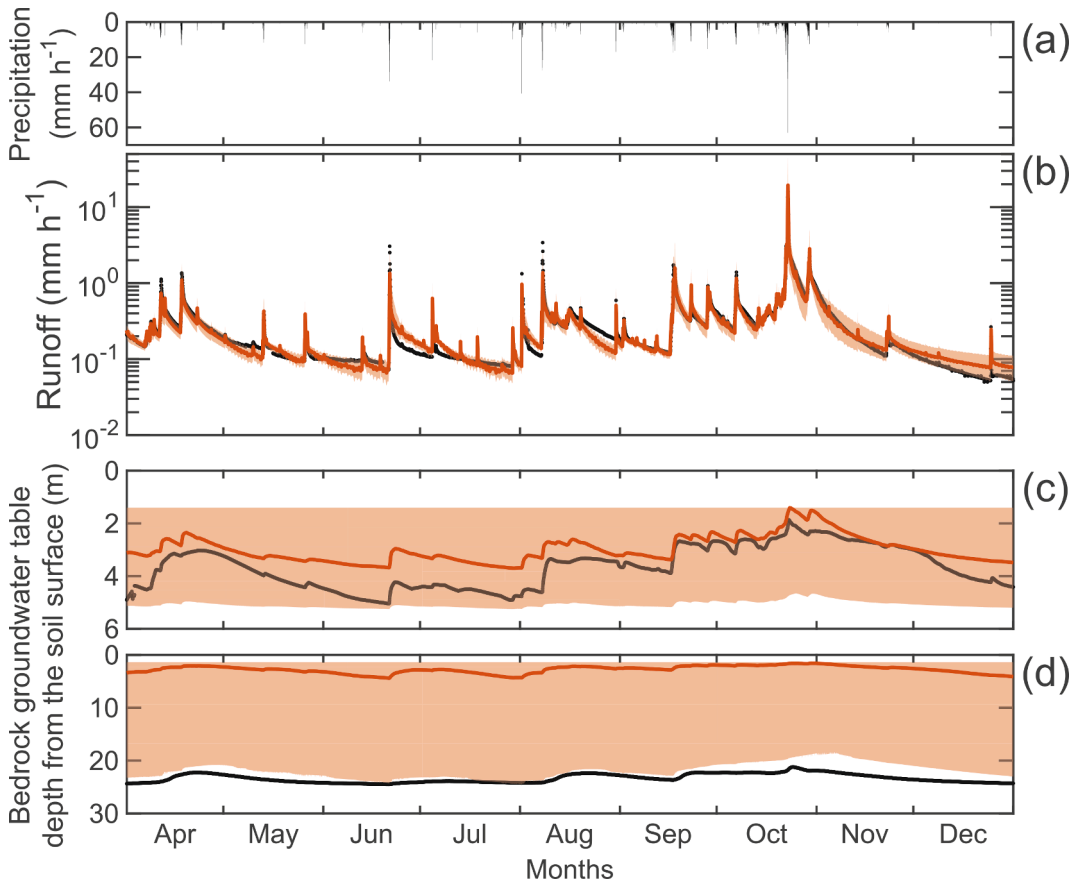

Fig. 7. Observations (black) and BL-S&B simulations (red curves with shading) of the catchment runoff and bedrock groundwater table depth in April–December 2017. (a) Hourly mean precipitation and (b) hourly mean runoff. Bedrock groundwater table depth measured from the soil surface at bedrock well locations (Fig. 3): (c) and (d) riparian zone (downslope) and upslope, respectively. Red curves represent the simulated median, with the shading indicating the 2.5 %–97.5 % percentile range. (For interpretation of the references to colour in this figure legend, the reader is referred to the web version of this article.)

absence of physical validity constraints on the calibrated parameters would become detrimental to understanding runoff generation (Gupta and Nearing, 2014).

In this study, we applied a Bayesian inference approach to parameterize the soil mantle and bedrock domains in the BLADE model. We obtained probability distributions for all model parameters instead of single values, allowing the model to also simulate spatial variations of the parameters (Figs. 4 and 5). Then, we compared the performance of the BL-S&B and BL-S model versions, which include and exclude, respectively, the effects of the bedrock model domain on runoff generation. Overall, catchment runoff reproducibility was lower in BL-S than in BL-S&B, particularly under low-flow conditions (Fig. 4).

Furthermore, the soil geophysical parameters retrieved with BL-S&B were reasonably consistent with observations, whereas BL-S parameter values, adjusted to reconcile runoff output between BL-S&B and BL-S, were physically unrealistic (Figs. 5 and 6). Similar results, where two catchment runoff models (one complex and one simple) produced comparable runoff output, but with very different soil characteristics derived from parameter optimization, were previously reported (Wen et al., 2021). We believe that the BL-S&B/BL-S comparison is an example of "equifinality" (Bahremand, 2016; Beven, 2006), when good model performance does not imply physical validity but might be obtained with parameter values outside the calibration range. This further emphasizes the necessity of implementing bedrock hydrology in realistic catchment runoff models. Here, in addition to realistic soil mantle characteristics, we also obtained a reasonable estimate of the saturated bedrock hydraulic conductivity (approximately 10^{-3} m h^{-1}), consistent with values representative of low unsaturated soil hydraulic conductivity reported in a previous study (Manning et al., 2021; Figs. 5 and 6). This confirms the importance of characterizing bedrock moisture movement for catchment runoff modeling.

Unlike previous analyses that used physically distributed hydrological models without a permeable bedrock domain, the full BL-S&B model version successfully reproduced low-flow runoff during dry periods (e.g. Ala-aho et al., 2017), further demonstrating the critical role of the bedrock hydrology submodel for low-flow runoff simulations.

5.2. *Importance of bedrock groundwater for mountain water resources*

Using the BLADE model, we successfully reproduced observations of, simultaneously, the catchment runoff and bedrock groundwater table depth at two slope positions (Fig. 7). This highly challenging simulation is the most innovative result of our study. Boring cores extracted from the upslope bedrock well (Fig. 3) exhibited frequent fissures and clay layers at depths of 20 m, 22–25 m, and 36–37 m (Yokoyama et al., 2013) that might allow bedrock groundwater to drain, thereby lowering the effective groundwater table depth and possibly resulting in a strong underestimation of the observed upslope groundwater table depth (Fig. 7c). The reported substantial spatial heterogeneity of bedrock hydraulic conductivity (Welch and Allen, 2014) would further degrade the consistency between the observed and modeled bedrock groundwater table depth. In this study, as a result of the simplified description of groundwater flow dynamics, we expected the simulated output to underestimate the observations; on the contrary, it corresponded reasonably well to the range of observed values, excluding spatial heterogeneity effects. For these reasons, the satisfactory reproduction of the observed multiple-peak catchment runoff (Fig. 7), possibly corresponding to bedrock groundwater table depth variations (Kosugi et al.,

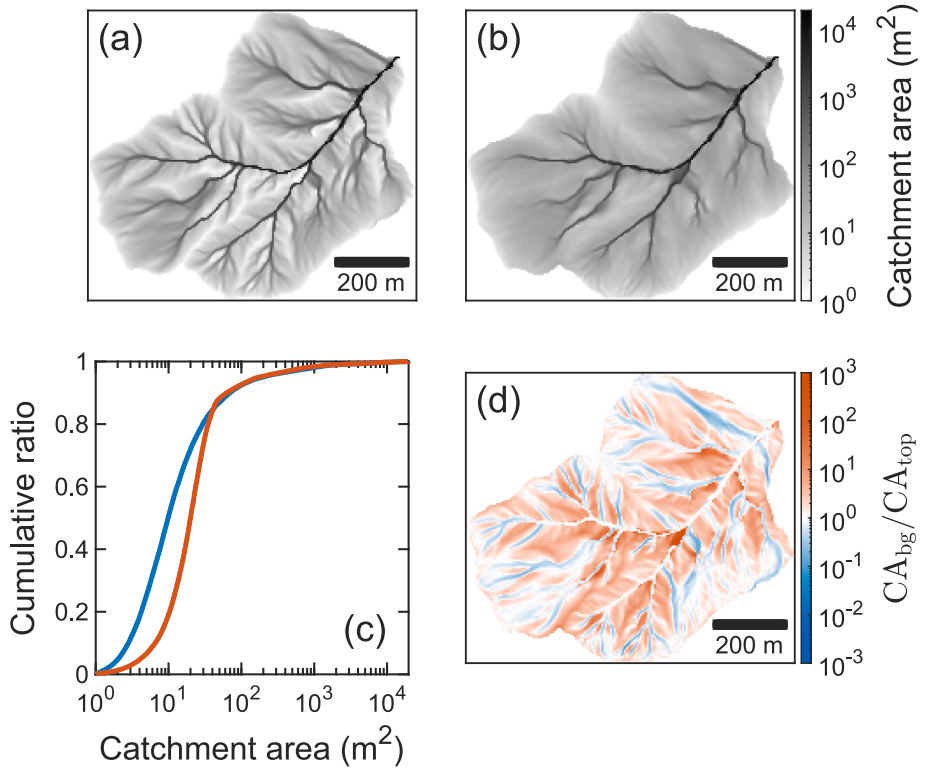

Fig. 8. Partial catchment area comparison. Top: spatial distributions calculated from (a) a digital elevation model of the ground surface topography (CA_{top}) and (b) the bedrock groundwater table depth simulated with BL-S&B on 19 September 2017 during a large rainfall event (CA_{bg}; total rainfall: 202 mm). Bottom: (c) cumulative ratio for CA_{top} (blue) and CA_{bg} (red) and (d) spatial distribution of the CA_{bg}/CA_{top} ratio, with values larger and smaller than 1 indicating rainfall collection primarily in the bedrock (CA_{bg}) or near soil surface (CA_{top}), respectively. (For interpretation of the references to colour in this figure legend, the reader is referred to the web version of this article.)

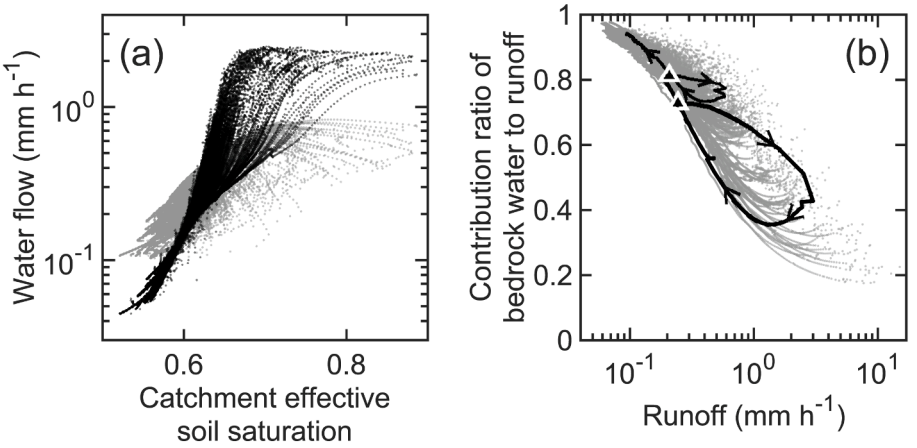

Fig. 9. Importance of bedrock groundwater flow dynamics for runoff generation. (a) Dependence of the bedrock infiltration (downward flow; black dots) and spring (upward flow; gray dots) rates at the soil–bedrock interface on the effective soil saturation. All data points (dots) represent catchment-mean parameter values simulated with BL-S&B. (b) Dependence of the contribution ratio of bedrock groundwater to the catchment runoff on the runoff itself (gray dots), exhibiting two hysteresis cycles (solid curves) with approximate periods of 14 days (small cycle) and 22 days (large cycle); the starting point (filled triangles) and direction of progress (arrows) are indicated. Both data are simulation outputs with BL-S&B.

2011), constitutes a notable achievement of the BLADE model.

Fig. 7 also suggests that groundwater table depth variations in the riparian zone were related to the stream runoff and propagated to the upslope area, as demonstrated in Voeckler et al. (2014). A stable groundwater flow, accumulating from broader areas to feed aquifers in the riparian zone, generates an excess of saturated overland flow along the stream channel that contributes to generating catchment runoff, even in dry periods (Fig. 8; Ala-aho et al., 2017; Partington et al., 2013). Additionally, incident rainfall, by expanding the groundwater exfiltration area to the upper slopes while maintaining saturated conditions in the riparian zone, as illustrated in Fig. 8, also contributes to the excess saturated overland flow (Soulsby et al., 2015).

As explained in Section 4.3, Fig. 9a illustrates the importance of infiltration and spring processes at the soil–bedrock interface (bedrock inflow–outflow) for catchment runoff generation, emphasized in previous publications (e.g. Spence and Woo, 2003). A common assumption is

that fractured and matric flows are the dominant mechanisms for moisture transport in sedimentary and granite bedrocks, respectively (Asano et al., 2023). A previous study (Onda et al., 2006) reported that subsurface stormflow occurs through the soil mantle in catchments with a nearly impermeable granite bedrock, but through the bedrock itself in catchments underlain by shale, a fractured sedimentary rock. Even for low-permeability, unfractured bedrock, recharge and bedrock infiltration might occur if catchment wetness is high (Gabrielli and McDonnell, 2018). In such a case, soil mantle thickness and hydraulic conductivity both affect the wetness conditions at the soil–bedrock interface, thereby controlling the bedrock infiltration rate (Gleeson et al., 2009).

In the OEW, the bedrock is composed of fractured sedimentary rock, where the saturated hydraulic conductivity is comparable to that of unsaturated soil in the catchment (Figs. 5 and 6). In our analysis, infiltration into the bedrock rapidly reached its maximum value when catchment wetness increased (Fig. 9a). Once the infiltration rate reached saturation, any additional rainfall could induce a rapid increase in the bedrock groundwater content, likely to immediately increase catchment runoff (Fig. 9b; Rempe and Dietrich, 2018). We also identified a dominant contribution of infiltration to bedrock reservoir replenishment during wet periods (Fig. 9a; Gabrielli and McDonnell, 2018; Rempe and Dietrich, 2018).

Under low-flow conditions, the bedrock groundwater contribution to the runoff exceeded approximately 80 %, suggesting that most catchment runoff occurred through the bedrock during dry periods (Fig. 9b; e.g. Uchida and Asano, 2010). Conversely, the contribution to the stormflow decreased with increasing catchment wetness and runoff because of bedrock saturation and high soil hydraulic conductivity at the soil–bedrock interface (Fig. 9b), as previously reported in observational studies (Uchida et al., 2003a, b). However, observations contradicting our results have also been reported in Asano et al. (2023), describing a sharp stormflow increase with increasing catchment wetness concurrent with an increase in the deeper groundwater contribution to runoff; this was attributed to a possible preferential flow path from the deep bedrock during large storms (Asano et al., 2023). To evaluate the plausibility of the simulated contribution of bedrock groundwater to streamflow, we compared it with baseflow estimates derived from conventional hydrograph separation methods (Appendix B, Fig. B.1). The comparison helps contextualize the simulated results within established empirical approaches.

Interestingly, BLADE successfully reproduced hysteresis in the catchment runoff generation processes (Fig. 9b). Systems exhibiting hysteresis are commonly characterized as possessing memory; that is, their current state depends on past properties and events (Gharari and Razavi, 2018). Simulating a catchment with memory, in principle, would require a complete understanding of all hydrological processes involved, their heterogeneity, and their spatiotemporal variations and representative scales (Gharari and Razavi, 2018). Because the simulated relationship between catchment runoff and bedrock groundwater contribution (Fig. 9b) depended on water storage in the bedrock and, implicitly, the soil mantle, it corresponded to different runoff values depending on the system status (i.e., wetting or drying period), yielding the clockwise hysteresis loops and dilution. This corresponds to the general case for concentration–discharge relationships of bedrock-derived solutes (House and Warwick, 1998; Rose et al., 2018). This result was not unexpected, because of the equivalence between bedrock groundwater contribution to runoff and concentration of bedrock-derived solutes in the runoff (Evans and Davies, 1998). This allowed us to simultaneously model hydrological processes in the soil mantle and the bedrock that involve multiple reservoirs and outflow sources, representative of systems with memory.

Bedrock reservoirs play a key role not only in regulating catchment runoff but also in supplying water to plants (Rempe and Dietrich, 2018). For example, most forest vegetation throughout the USA has direct access to root-zone bedrock water storage, which constitutes a critical ecosystem water resource (McCormick et al., 2021).

In particular, analyzing hydrological processes at the soil–bedrock interface is essential to better understand the influence of transient groundwater, transported through the hillslope–riparian zone–valley topographic system, on catchment runoff generation (Camporese et al., 2019). The precise effects of hydraulic conductivity in a fractured bedrock on water flow dynamics remain incompletely characterized. This open scientific question requires extensive and technically challenging observations (Kosugi et al., 2011) and theoretical analyses (Broda et al., 2011). It is a promising research topic for water resource science in mountainous environments.

6. Conclusion

We developed BLADE, a novel physically-based distributed hydrological model that fully accounts for bedrock hydrology. By applying BLADE to an intensively monitored mountain headwater catchment, we successfully reproduced observations of catchment runoff and bedrock groundwater table depth, as well as soil moisture dynamics. A Bayesian inference approach allowed us to estimate posterior probability distributions for physically meaningful parameters in both the soil and the bedrock domains, leading to realistic representations of catchment hydrological processes.

Comparison between the full BLADE configuration (BL-S&B) and a simplified version without bedrock hydrology (BL-S) revealed that neglecting bedrock processes degrades model performance, particularly under low-flow conditions. Furthermore, the BL-S configuration yielded physically unrealistic soil parameters despite similar runoff simulations—an example of equifinality—because it overestimated the effective soil porosity and underestimated the saturated soil hydraulic conductivity. Moreover, because BLADE is able to simulate a bedrock groundwater table surface distinct from the ground surface topography, the model was able to represent the spatiotemporal runoff generation processes and reproduce baseflow.

This study demonstrates the dominant role of bedrock groundwater in runoff generation during low-flow periods and the importance of infiltration and spring processes at the soil–bedrock interface for controlling stormflow and baseflow. These findings emphasize that realistic representation of bedrock hydrology is essential for understanding and predicting runoff generation in mountain headwater catchments, and they provide a foundation for improving water resource management in forested mountain catchments, with BLADE representing a promising tool to support such applications.

CRediT authorship contribution statement

Toshiaki Kameyama: Writing – original draft, Visualization, Software, Methodology, Funding acquisition, Formal analysis, Conceptualization. **Tomo'omi Kumagai:** Writing – original draft, Supervision, Project administration, Funding acquisition, Conceptualization. **Tomohiro Egusa:** Writing – review & editing, Investigation, Data curation. **Hiroki Momiyama:** Writing – review & editing, Investigation, Data curation.

Declaration of competing interest

The authors declare that they have no known competing financial interests or personal relationships that could have appeared to influence the work reported in this paper.

Acknowledgments

The authors thank the staff of the Kanagawa Prefectural Government for logistical support in conducting observations throughout the Oborasawa Experimental Watershed (OEW) and members of Forest Biogeosciences Lab (The University of Tokyo) for fieldwork, especially Naoya Fujime and Tomoki Oda. This work was partly achieved through

the use of large-scale computer systems (SQUID) at the Cybermedia Center, Osaka University. We thank Eric Dupuy, from Edanz (https://jp.edanz.com/ac), for editing a draft of this manuscript.

Funding sources

The funding for this work was supported by the Kanagawa Prefectural Government, Japan, as part of the project on "Forest, soil, and water resource conservation in the western Kanagawa reservoir area"; by Grants-in-Aid for Scientific Research [grant numbers 20KK0140, 22J12319, 22KJ0853] from the Ministry of Education, Culture, Sports, Science and Technology, Japan; and by the Support for Pioneering Research Initiated by the Next Generation (SPRING) program of the Japan Science and Technology Agency (JST), Japan [grant number JPMJSP2108].

Appendix A. Geophysical and model parameters used for BLADE simulations

Symbol	Unit	Definition
b		Soil pore size distribution index
c		Soil pore disconnectedness index
D	m	Model soil block height
I_c	m h^{-1}	Canopy interception rate
K	m h^{-1}	Soil hydraulic conductivity
K_{sat}	m h^{-1}	Saturated soil hydraulic conductivity
$K_{rc,lsat}$	m h^{-1}	Saturated bedrock hydraulic conductivity for lateral flow
$K_{rc,lsat\_0}$	m h^{-1}	Value of $K_{rc,lsat}$ in the topmost bedrock region
$K_{rc,vsat}$	m h^{-1}	Saturated bedrock hydraulic conductivity for vertical flow
f_{rc}	m^{-1}	Attenuation factor defining the dependence of $K_{rc,lsat}$ on depth z
l	m	Horizontal distance to the adjacent downstream block
L	m	Soil block horizontal length
NSE		Nash-Sutcliffe efficiency
NSE_{inv}		NSE calculated with inverse Q values
NSE_{ln}		NSE calculated with the natural logarithm of Q values
NSE_o		Ordinary NSE
p_{ac}		Acceptance probability (ratio between NSE values for consecutive iterations)
P_e	m h^{-1}	Effective rainfall rate (gross rainfall minus canopy interception)
P_g	m h^{-1}	Gross rainfall rate
$q_{sl,inf}$	m h^{-1}	Infiltration rate at the soil surface
$q_{rc,inf}$, $q_{rc,sp}$	m h^{-1}	Vertical water inflow (infiltration) and outflow (spring) rates at the soil–bedrock interface
Q	Arbitrary	Runoff
Q_m	Arbitrary	Simulated runoff
Q_o	Arbitrary	Observed runoff
$Q_{ov,in}$, $Q_{ov,out}$	m h^{-1}	Overland water inflow and outflow rates for a soil block
Q_{Hort}	m h^{-1}	Hortonian overland water flow
Q_{ret}	m h^{-1}	Return water flow
$Q_{sl,in}$, $Q_{sl,out}$	m^3 h^{-1}	Lateral soil water inflow and outflow rates for a soil block
$Q_{rc,in}$, $Q_{rc,out}$	m^3 h^{-1}	Lateral bedrock water inflow and outflow rates for a bedrock block
r_{IC}		Vegetation interception ratio
R_n	W m^{-2}	Net radiation
SIC	m h^{-1}	Soil infiltration capacity
S_e		Effective soil saturation
$\langle S_e \rangle$		Catchment-mean effective soil saturation
S_p	m h$^{-0.5}$	Sorptivity (0.035 m h$^{-0.5}$)
t_p	h	Sorption duration
T_r	m h^{-1}	Transpiration rate
W	m	Soil block cross-section width normal to the water flow direction
x	m	Position along the slope (positive in the downslope direction)
$\mathbb{X}$		Vector of prior parameters (see text for list)
z	m	Depth from the ground surface
z_{ae}	m	Depth at the air entry pressure
z_{gw}	m	Groundwater table depth
α		Priestley–Taylor coefficient
α_{soil}		Contribution ratio of bedrock water to soil water storage
α_{surf}		Contribution ratio of bedrock water to surface water flow
γ	Pa K^{-1}	Psychrometric constant (62 Pa K^{-1})
δ	Pa K^{-1}	Slope of the saturation water vapor pressure curve
Θ	m^3 m^{-3}	Mean volumetric water content in a soil block
θ	m^3 m^{-3}	Soil volumetric water content
θ_r	m^3 m^{-3}	Residual soil volumetric water content
θ_s	m^3 m^{-3}	Soil porosity
λ	J kg^{-1}	Latent heat of water vaporization (2.4 × 10^6 J kg^{-1})
ρ_w	kg m^{-3}	Water density
ϕ_{rc}	m^3 m^{-3}	Bedrock porosity
ψ	m	Soil water pressure head
ψ_{ae}	m	Air entry water pressure head
ψ_{sb}	m	Water pressure head at the soil–bedrock interface
Ψ	m	Mean water pressure head in a soil block
Ψ_1, Ψ_2		Values of Ψ in a soil block and the adjacent downstream block
ω		Local slope of the soil–bedrock interface
ω_{gw}		Local slope of the groundwater table

Appendix B. Comparison with conventional baseflow separation methods

To evaluate the contribution of bedrock groundwater simulated by BL-S&B to catchment runoff, we performed a hydrograph separation using the grwat package in R (Samsonov, 2024), which implements several conventional baseflow segmentation methods. This allowed qualitative comparison between the bedrock groundwater contribution simulated by BL-S&B and the baseflow estimated from observed hourly runoff.

We applied four widely used methods: Lyne and Hollick (1979), Boughton (1993), Jakeman and Hornberger (1993), and Chapman and Maxwell (1996), and for each method, we used the default filtering parameters provided in the grwat package, i.e., 0.925, 0.975, 0.925, and 0.975, respectively.

The estimated baseflow hydrographs obtained from these methods exhibited notable differences in magnitude and timing depending on the algorithm used. Compared with these empirical estimations, BL-S&B simulations captured the general magnitude and temporal patterns of baseflow reasonably well, particularly during low-flow periods (Fig. B.1).

However, it should be noted that the results of conventional baseflow segmentation methods are sensitive to methodological choices, and that their outcomes are not fully consistent with each other. Moreover, baseflow does not necessarily correspond exclusively to bedrock groundwater contributions and, conversely, not all bedrock groundwater contributions are necessarily captured as baseflow—some might be included in the estimated quickflow. Therefore, this comparison should be regarded as qualitative, and the limitations inherent in both approaches must be acknowledged when interpreting the results.

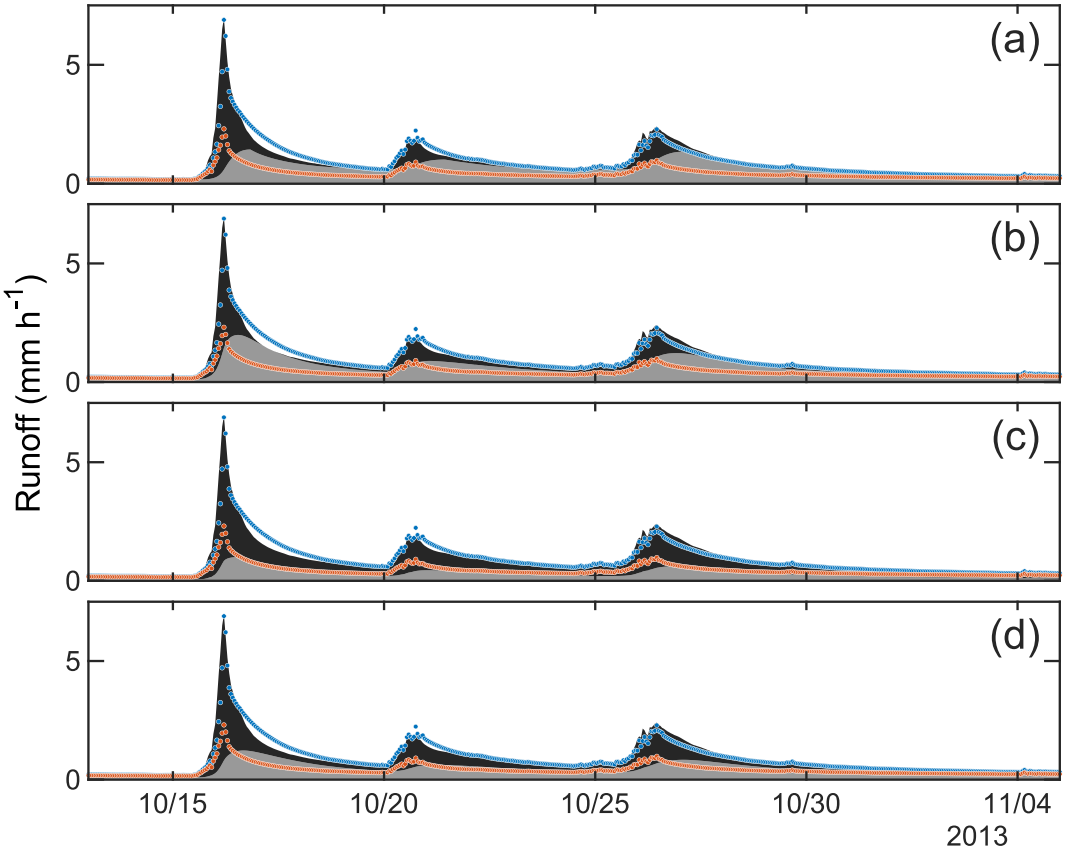

Fig. B1. Comparison of the bedrock groundwater contribution simulated by BL-S&B (red) with conventional hydrograph separation methods. The total runoff simulated by BL-S&B (blue) is indicated for reference. Baseflow (gray shading) and quickflow (black shading) are segmented using the (a) Lyne and Hollick (1979), (b) Boughton (1993), (c) Jakeman and Hornberger (1993), and (d) Chapman and Maxwell (1996) methods.

Data availability

Data will be made available on request.

References

Ala-aho, P., Soulsby, C., Wang, H., Tetzlaff, D., 2017. Integrated surface-subsurface model to investigate the role of groundwater in headwater catchment runoff generation: a minimalist approach to parameterisation. J. Hydrol. 547, 664–677. https://doi.org/10.1016/j.jhydrol.2017.02.023.

Ameli, A.A., Craig, J.R., McDonnell, J.J., 2015. Are all runoff processes the same? Numerical experiments comparing a Darcy-Richards solver to an overland flow-based approach for subsurface storm runoff simulation. Water Resour. Res. 51, 10008–10028. https://doi.org/10.1002/2015WR017199.

Andréassian, V., 2004. Waters and forests: from historical controversy to scientific debate. J. Hydrol. 291, 1–27. https://doi.org/10.1016/j.jhydrol.2003.12.015.

Asano, Y., Kawasaki, M., Takatoku, K., Uchida, T., Hiroki, S., 2023. Lateral flow in bedrock dominates baseflow and flood flow in a catchment underlain with permeable sedimentary rock in the high-relief Chichibu Mountains. Hydrol. Process. 37, e15011. https://doi.org/10.1002/hyp.15011.

Bahremand, A., 2016. HESS opinions: advocating process modeling and de-emphasizing parameter estimation. Hydrol. Earth Syst. Sci. 20, 1433–1445. https://doi.org/10.5194/hess-20-1433-2016.

Beven, K., 2006. A manifesto for the equifinality thesis. J. Hydrol. 320, 18–36. https://doi.org/10.1016/j.jhydrol.2005.07.007.

Beven, K., 1981. Kinematic subsurface stormflow. Water Resour. Res. 17, 1419–1424. https://doi.org/10.1029/WR017i005p01419.

Beven, K.J., Kirkby, M.J., 1979. A physically based, variable contributing area model of basin hydrology. Hydrol. Sci. Bull. 24, 43–69. https://doi.org/10.1080/02626667909491834.

Boughton, W.C., 1993. A hydrograph-based model for estimating the water yield of ungauged catchments, in: Hydrology and Water Resources Symposium, Newcastle, Institution of Engineers Australia. pp. 317–324.

Broda, S., Paniconi, C., Larocque, M., 2011. Numerical investigation of leakage in sloping aquifers. J. Hydrol. 409, 49–61. https://doi.org/10.1016/j.jhydrol.2011.07.035.
Brooks, R.H., Corey, A.T., 1964. Hydraulic properties of porous media and their relation to drainage design. Trans. ASAE 7, 26–28. https://doi.org/10.13031/2013.40684.
Burns, D.A., Murdoch, P.S., Lawrence, G.B., Michel, R.L., 1998. Effect of groundwater springs on NO_3^- concentrations during summer in Catskill Mountain streams. Water Resour. Res. 34, 1987–1996. https://doi.org/10.1029/98WR01282.
Camporese, M., Paniconi, C., Putti, M., McDonnell, J.J., 2019. Fill and spill hillslope runoff representation with a Richards equation-based model. Water Resour. Res. 55, 8445–8462. https://doi.org/10.1029/2019WR025726.
Chapman, T.G., Maxwell, A.I., 1996. Baseflow separation - comparison of numerical methods with tracer experiments, in: Hydrology and Water Resources Symposium 1996: Water and the Environment; Preprints of Papers. pp. 539–545. https://doi.org/10.3316/informit.360361071346753.
Criss, R.E., Winston, W.E., 2008. Do Nash values have value? Discussion and alternate proposals. Hydrol. Process. 22, 2723–2725. https://doi.org/10.1002/hyp.7072.
David, G.C.L., Wohl, E., Yochum, S.E., Bledsoe, B.P., 2010. Controls on spatial variations in flow resistance along steep mountain streams. Water Resour. Res. 46. https://doi.org/10.1029/2009WR008134.
Egusa, T., Oda, T., Sato, T., Kumagai, T., 2021. Estimation of sub-annual inter-catchment groundwater flow using short-term water balance method. Hydrol. Process. 35, e14368. https://doi.org/10.1002/hyp.14368.
Evans, C., Davies, T.D., 1998. Causes of concentration/discharge hysteresis and its potential as a tool for analysis of episode hydrochemistry. Water Resour. Res. 34, 129–137. https://doi.org/10.1029/97WR01881.
Fujimoto, M., Ohte, N., Kawasaki, M., Osaka, K., Itoh, M., Ohtsuka, I., Itoh, M., 2016. Influence of bedrock groundwater on streamflow characteristics in a volcanic catchment. Hydrol. Process. 30, 558–572. https://doi.org/10.1002/hyp.10558.
Gabrielli, C.P., McDonnell, J.J., 2018. No direct linkage between event-based runoff generation and groundwater recharge on the Maimai hillslope. Water Resour. Res. 54, 8718–8733. https://doi.org/10.1029/2017WR021831.
Gharari, S., Razavi, S., 2018. A review and synthesis of hysteresis in hydrology and hydrological modeling: memory, path-dependency, or missing physics? J. Hydrol. 566, 500–519. https://doi.org/10.1016/j.jhydrol.2018.06.037.
Gleeson, T., Novakowski, K., Kurt Kyser, T., 2009. Extremely rapid and localized recharge to a fractured rock aquifer. J. Hydrol. 376, 496–509. https://doi.org/10.1016/j.jhydrol.2009.07.056.
Grant, G.E., Tague, C.L., Allen, C.D., 2013. Watering the forest for the trees: an emerging priority for managing water in forest landscapes. Front. Ecol. Environ. 11, 314–321. https://doi.org/10.1890/120209.
Gupta, H.V., Nearing, G.S., 2014. Debates—the future of hydrological sciences: a (common) path forward? Using models and data to learn: a systems theoretic perspective on the future of hydrological science. Water Resour. Res. 50, 5351–5359. https://doi.org/10.1002/2013WR015096.
House, W.A., Warwick, M.S., 1998. Hysteresis of the solute concentration/discharge relationship in rivers during storms. Water Res. 32, 2279–2290. https://doi.org/10.1016/S0043-1354(97)00473-9.
Hrachowitz, M., Clark, M.P., 2017. HESS opinions: the complementary merits of competing modelling philosophies in hydrology. Hydrol. Earth Syst. Sci. 21, 3953–3973. https://doi.org/10.5194/hess-21-3953-2017.
Iwasaki, K., Katsuyama, M., Tani, M., 2015. Contributions of bedrock groundwater to the upscaling of storm-runoff generation processes in weathered granitic headwater catchments. Hydrol. Process. 29, 1535–1548. https://doi.org/10.1002/hyp.10279.
Jakeman, A.J., Hornberger, G.M., 1993. How much complexity is warranted in a rainfall-runoff model? Water Resour. Res. 29, 2637–2649. https://doi.org/10.1029/93WR00877.
Japanese Geotechnical Society, 2003. JGS 1321 – Method for determination of hydraulic properties of rock mass using instantaneous head recovery technique in single borehole. (in Japanese).
Katsura, S., Kosugi, K., Mizutani, T., Okunaka, S., Mizuyama, T., 2008. Effects of bedrock groundwater on spatial and temporal variations in soil mantle groundwater in a steep granitic headwater catchment. Water Resour. Res. 44, W09430. https://doi.org/10.1029/2007WR006610.
Katsura, S., Kosugi, K., Yamamoto, N., Mizuyama, T., 2006. Saturated and unsaturated hydraulic conductivities and water retention characteristics of weathered granitic bedrock. Vadose Zone J. 5, 35–47. https://doi.org/10.2136/vzj2005.0040.
Komatsu, H., Tanaka, N., Kume, T., 2007. Do coniferous forests evaporate more water than broad-leaved forests in Japan? J. Hydrol. 336, 361–375. https://doi.org/10.1016/j.jhydrol.2007.01.009.
Kosugi, K., Fujimoto, M., Katsura, S., Kato, H., Sando, Y., Mizuyama, T., 2011. Localized bedrock aquifer distribution explains discharge from a headwater catchment. Water Resour. Res. 47, W07530. https://doi.org/10.1029/2010WR009884.
Kosugi, K., Katsura, S., Katsuyama, M., Mizuyama, T., 2006. Water flow processes in weathered granitic bedrock and their effects on runoff generation in a small headwater catchment. Water Resour. Res. 42, W02414. https://doi.org/10.1029/2005WR004275.
Kosugi, K., Katsura, S., Mizuyama, T., Okunaka, S., Mizutani, T., 2008. Anomalous behavior of soil mantle groundwater demonstrates the major effects of bedrock groundwater on surface hydrological processes. Water Resour. Res. 44, W01407. https://doi.org/10.1029/2006WR005859.
Krause, P., Boyle, D.P., Bäse, F., 2005. Comparison of different efficiency criteria for hydrological model assessment. Adv. Geosci. 5, 89–97. https://doi.org/10.5194/adgeo-5-89-2005.
Kubota, J., Fukushima, Y., Suzuki, M., 1988. Observation and modeling of the runoff process on a hillslope (II) Water budget and location of the groundwater table and its rising. J. Jpn For. Soc. 70, 381–389. https://doi.org/10.11519/jjfs1953.70.9_381 in Japanese with English abstract.
Kubota, J., Fukushima, Y., Suzuki, M., 1987. Observation and modeling of the runoff process on a hillslope. J. Jpn For. Soc. 69, 258–269. https://doi.org/10.11519/jjfs1953.69.7_258 in Japanese with English abstract.
Kubota, J., Sivapalan, M., 1995. Towards a catchment-scale model of subsurface runoff generation based on synthesis of small-scale process-based modelling and field studies. Hydrol. Process. 9, 541–554. https://doi.org/10.1002/hyp.3360090506.
Kumagai, T., Katul, G.G., Porporato, A., Saitoh, T.M., Ohashi, M., Ichie, T., Suzuki, M., 2004. Carbon and water cycling in a Bornean tropical rainforest under current and future climate scenarios. Adv. Water Resour. 27, 1135–1150. https://doi.org/10.1016/j.advwatres.2004.10.002.
Kumagai, T., Tateishi, M., Miyazawa, Y., Kobayashi, M., Yoshifuji, N., Komatsu, H., Shimizu, T., 2014. Estimation of annual forest evapotranspiration from a coniferous plantation watershed in Japan (1): Water use components in Japanese cedar stands. J. Hydrol. 508, 66–76. https://doi.org/10.1016/j.jhydrol.2013.10.047.
Kumagai, T., Tateishi, M., Shimizu, T., Otsuki, K., 2008. Transpiration and canopy conductance at two slope positions in a Japanese cedar forest watershed. Agric. For. Meteorol. 148, 1444–1455. https://doi.org/10.1016/j.agrformet.2008.04.010.
Lanni, C., McDonnell, J., Hopp, L., Rigon, R., 2013. Simulated effect of soil depth and bedrock topography on near-surface hydrologic response and slope stability. Earth Surf. Proc. Land. 38, 146–159. https://doi.org/10.1002/esp.3267.
Lyne, V., Hollick, M., 1979. Stochastic time-variable rainfall-runoff modeling. Aust. Natl. Conf. Publ. 89–92.
Manning, A.H., Ball, L.B., Wanty, R.B., Williams, K.H., 2021. Direct observation of the depth of active groundwater circulation in an alpine watershed. Water Resour. Res. 57, e2020WR028548. https://doi.org/10.1029/2020WR028548.
Masaoka, N., Kosugi, K., Fujimoto, M., 2021. Bedrock groundwater catchment area unveils rainfall-runoff processes in headwater basins. Water Resour. Res. 57, e2021WR029888. https://doi.org/10.1029/2021WR029888.
McCormick, E.L., Dralle, D.N., Hahm, W.J., Tune, A.K., Schmidt, L.M., Chadwick, K.D., Rempe, D.M., 2021. Widespread woody plant use of water stored in bedrock. Nature 597, 225–229. https://doi.org/10.1038/s41586-021-03761-3.
McDonnell, J.J., Evaristo, J., Bladon, K.D., Buttle, J., Creed, I.F., Dymond, S.F., Grant, G., Iroume, A., Jackson, C.R., Jones, J.A., Maness, T., McGuire, K.J., Scott, D.F., Segura, C., Sidle, R.C., Tague, C., 2018. Water sustainability and watershed storage. Nat. Sustain. 1, 378–379. https://doi.org/10.1038/s41893-018-0099-8.
Momiyama, H., Kumagai, T., Egusa, T., 2019. Reproducing monthly evapotranspiration from a coniferous plantation watershed in Japan. J. For. Res. 24, 197–200. https://doi.org/10.1080/13416979.2019.1604606.
Momiyama, H., Kumagai, T., Fujime, N., Egusa, T., Shimizu, T., 2023. Forest canopy interception can reduce flood discharge: inferences from model assumption analysis. J. Hydrol. 623, 129843. https://doi.org/10.1016/j.jhydrol.2023.129843.
Moreno, H.A., Gupta, H.V., White, D.D., Sampson, D.A., 2016. Modeling the distributed effects of forest thinning on the long-term water balance and streamflow extremes for a semi-arid basin in the southwestern US. Hydrol. Earth Syst. Sci. 20, 1241–1267. https://doi.org/10.5194/hess-20-1241-2016.
Nash, J.E., Sutcliffe, J.V., 1970. River flow forecasting through conceptual models part I — a discussion of principles. J. Hydrol. 10, 282–290. https://doi.org/10.1016/0022-1694(70)90255-6.
Oda, T., Suzuki, M., Egusa, T., Uchiyama, Y., 2013. Effect of bedrock flow on catchment rainfall-runoff characteristics and the water balance in forested catchments in Tanzawa Mountains, Japan. Hydrol. Process. 27, 3864–3872. https://doi.org/10.1002/hyp.9497.
Onda, Y., Tsujimura, M., Fujihara, J., Ito, J., 2006. Runoff generation mechanisms in high-relief mountainous watersheds with different underlying geology. J. Hydrol. 331, 659–673. https://doi.org/10.1016/j.jhydrol.2006.06.009.
Padilla, C., Onda, Y., Iida, T., 2015. Interaction between runoff – bedrock groundwater in a steep headwater catchment underlain by sedimentary bedrock fractured by gravitational deformation. Hydrol. Process. 29, 4398–4412. https://doi.org/10.1002/hyp.10498.
Partington, D., Brunner, P., Frei, S., Simmons, C.T., Werner, A.D., Therrien, R., Maier, H. R., Dandy, G.C., Fleckenstein, J.H., 2013. Interpreting streamflow generation mechanisms from integrated surface-subsurface flow models of a riparian wetland and catchment. Water Resour. Res. 49, 5501–5519. https://doi.org/10.1002/wrcr.20405.
Philip, J.R., 1957a. The theory of infiltration: 1. The infiltration equation and its solution. Soil Sci. 83, 345–358. https://doi.org/10.1097/00010694-195705000-00002.
Philip, J.R., 1957b. The theory of infiltration: 4. Sorptivity and algebraic infiltration equations. Soil Sci. 84, 257–264. https://doi.org/10.1097/00010694-195709000-00010.
Priestley, C.H.B., Taylor, R.J., 1972. On the assessment of surface heat flux and evaporation using large-scale parameters. Mon. Weather Rev. 100, 81–92. https://doi.org/10.1175/1520-0493(1972)100<0081:OTAOSH>2.3.CO;2.
Pushpalatha, R., Perrin, C., Le Moine, N., Andréassian, V., 2012. A review of efficiency criteria suitable for evaluating low-flow simulations. J. Hydrol. 420–421, 171–182. https://doi.org/10.1016/j.jhydrol.2011.11.055.
Quinn, P., Beven, K., Chevallier, P., Planchon, O., 1991. The prediction of hillslope flow paths for distributed hydrological modelling using digital terrain models. Hydrol. Process. 5, 59–79. https://doi.org/10.1002/hyp.3360050106.
Rempe, D.M., Dietrich, W.E., 2018. Direct observations of rock moisture, a hidden component of the hydrologic cycle. Proc. Natl. Acad. Sci. 115, 2664–2669. https://doi.org/10.1073/pnas.1800141115.
Rose, L.A., Karwan, D.L., Godsey, S.E., 2018. Concentration–discharge relationships describe solute and sediment mobilization, reaction, and transport at event and

longer timescales. Hydrol. Process. 32, 2829–2844. https://doi.org/10.1002/hyp.13235.
Samsonov, T., 2024. grwat: River Hydrograph Separation and Analysis. R package version 0.0.4.9000, https://tsamsonov.github.io/grwat/, https://github.com/tsamsonov/grwat.
Seibert, J., Bishop, K., Nyberg, L., Rodhe, A., 2011. Water storage in a till catchment. I: distributed modelling and relationship to runoff. Hydrol. Process. 25, 3937–3949. https://doi.org/10.1002/hyp.8309.
Semenova, O., Beven, K., 2015. Barriers to progress in distributed hydrological modelling. Hydrol. Process. 29, 2074–2078. https://doi.org/10.1002/hyp.10434.
Somers, L.D., McKenzie, J.M., 2020. A review of groundwater in high mountain environments. WIREs Water 7, e1475. https://doi.org/10.1002/wat2.1475.
Soulsby, C., Birkel, C., Geris, J., Dick, J., Tunaley, C., Tetzlaff, D., 2015. Stream water age distributions controlled by storage dynamics and nonlinear hydrologic connectivity: modeling with high-resolution isotope data. Water Resour. Res. 51, 7759–7776. https://doi.org/10.1002/2015WR017888.
Spence, C., Woo, M., 2003. Hydrology of subarctic Canadian shield: soil-filled valleys. J. Hydrol. 279, 151–166. https://doi.org/10.1016/S0022-1694(03)00175-6.
Staudinger, M., Stoelzle, M., Cochand, F., Seibert, J., Weiler, M., Hunkeler, D., 2019. Your work is my boundary condition!: challenges and approaches for a closer collaboration between hydrologists and hydrogeologists. J. Hydrol. 571, 235–243. https://doi.org/10.1016/j.jhydrol.2019.01.058.
Talsma, T., 1969. In situ measurement of sorptivity. Soil Res. 7, 269–276. https://doi.org/10.1071/sr9690269.
Tani, M., 2008. Analysis of runoff–storage relationships to evaluate the runoff-buffering potential of a sloping permeable domain. J. Hydrol. 360, 132–146. https://doi.org/10.1016/j.jhydrol.2008.07.023.
Tromp-van Meerveld, H.J., Peters, N.E., McDonnell, J.J., 2007. Effect of bedrock permeability on subsurface stormflow and the water balance of a trenched hillslope at the Panola Mountain Research Watershed, Georgia, USA. Hydrol. Process. 21, 750–769. https://doi.org/10.1002/hyp.6265.
Tromp-van Meerveld, I., Weiler, M., 2008. Hillslope dynamics modeled with increasing complexity. J. Hydrol. 361, 24–40. https://doi.org/10.1016/j.jhydrol.2008.07.019.
Uchida, T., Asano, Y., 2010. Spatial variability in the flowpath of hillslope runoff and streamflow in a meso-scale catchment. Hydrol. Process. 24, 2277–2286. https://doi.org/10.1002/hyp.7767.
Uchida, T., Asano, Y., Ohte, N., Mizuyama, T., 2003a. Analysis of flowpath dynamics in a steep unchannelled hollow in the Tanakami Mountains of Japan. Hydrol. Process. 17, 417–430. https://doi.org/10.1002/hyp.1133.
Uchida, T., Asano, Y., Ohte, N., Mizuyama, T., 2003b. Seepage area and rate of bedrock groundwater discharge at a granitic unchanneled hillslope. Water Resour. Res. 39, 1018. https://doi.org/10.1029/2002WR001298.
Viviroli, D., Dürr, H.H., Messerli, B., Meybeck, M., Weingartner, R., 2007. Mountains of the world, water towers for humanity: typology, mapping, and global significance. Water Resour. Res. 43, W07447. https://doi.org/10.1029/2006WR005653.
Viviroli, D., Kummu, M., Meybeck, M., Kallio, M., Wada, Y., 2020. Increasing dependence of lowland populations on mountain water resources. Nat. Sustain. 3, 917–928. https://doi.org/10.1038/s41893-020-0559-9.
Voeckler, H.M., Allen, D.M., Alila, Y., 2014. Modeling coupled surface water – groundwater processes in a small mountainous headwater catchment. J. Hydrol. 517, 1089–1106. https://doi.org/10.1016/j.jhydrol.2014.06.015.
Welch, L.A., Allen, D.M., 2014. Hydraulic conductivity characteristics in mountains and implications for conceptualizing bedrock groundwater flow. Hydrgeol. J. 22, 1003–1026. https://doi.org/10.1007/s10040-014-1121-5.
Wen, H., Brantley, S.L., Davis, K.J., Duncan, J.M., Li, L., 2021. The limits of homogenization: what hydrological dynamics can a simple model represent at the catchment scale? Water Resour. Res. 57, e2020WR029528. https://doi.org/10.1029/2020WR029528.
Wigmosta, M.S., Vail, L.W., Lettenmaier, D.P., 1994. A distributed hydrology-vegetation model for complex terrain. Water Resour. Res. 30, 1665–1679. https://doi.org/10.1029/94WR00436.
Yokoyama, T., Uchiyama, Y., Satou, S., Yamane, M., 2013. Hydrogeological features of 4 experimental watersheds in the water resources protection area. Bull. Kanagawa Prefect. Nat. Environ. Conserv. Cent. 10, 203–214 in Japanese.
Zhang, Y., Deng, L., Yan, W., Shangguan, Z., 2016. Interaction of soil water storage dynamics and long-term natural vegetation succession on the Loess Plateau, China. Catena 137, 52–60. https://doi.org/10.1016/j.catena.2015.08.016.